

# RING#: PR-by-PE Global Localization with Roto-translation Equivariant Gram Learning

Sha Lu<sup>1</sup>, Xuecheng Xu<sup>1</sup>, Yuxuan Wu<sup>2</sup>, Haojian Lu<sup>1</sup>, Xieyuanli Chen<sup>3</sup>, Rong Xiong<sup>1</sup> and Yue Wang<sup>1†</sup>

arXiv:2409.00206v1 [cs.CV] 30 Aug 2024

**Abstract**—Global localization using onboard perception sensors, such as cameras and LiDARs, is crucial in autonomous driving and robotics applications when GPS signals are unreliable. Most approaches achieve global localization by sequential place recognition and pose estimation. Some of them train separate models for each task, while others employ a single model with dual heads, trained jointly with separate task-specific losses. However, the accuracy of localization heavily depends on the success of place recognition, which often fails in scenarios with significant changes in viewpoint or environmental appearance. Consequently, this renders the final pose estimation of localization ineffective. To address this, we propose a novel paradigm, *PR-by-PE localization*, which improves global localization accuracy by deriving place recognition directly from pose estimation. Our framework, RING#, is an end-to-end *PR-by-PE localization* network operating in the bird’s-eye view (BEV) space, designed to support both vision and LiDAR sensors. It introduces a theoretical foundation for learning two equivariant representations from BEV features, which enables globally convergent and computationally efficient pose estimation. Comprehensive experiments on the NCLT and Oxford datasets across both vision and LiDAR modalities demonstrate that our method outperforms state-of-the-art approaches. Furthermore, we provide extensive analyses to confirm the effectiveness of our method. The code will be publicly released.

**Index Terms**—Global Localization, Place Recognition, BEV Representation Learning, Roto-translation Equivariance.

## I. INTRODUCTION

**G**LOBAL localization is a fundamental task in autonomous driving and mobile robot navigation systems. The need for global localization arises when GPS signals are unavailable or inaccurate, such as indoor and urban canyons. It also enables loop closures in SLAM [1]–[5], recovers the current pose of kidnapped robots, and merges multi-robot/multi-session maps. To achieve global localization, we must register the current sensor observation against the entire map without prior knowledge.

Traditional global localization approaches, originating from early visual methods [3], [6], [7], typically follow a paradigm: first place recognition (PR) then pose estimation (PE). This paradigm, referred to as *PR-then-PE localization*, treats place recognition and pose estimation as upstream and downstream tasks, as illustrated in Fig. 1(a). Place recognition [8]–[17] retrieves a set of candidate keyframes from the map that are similar to the current observation, thereby narrowing the search

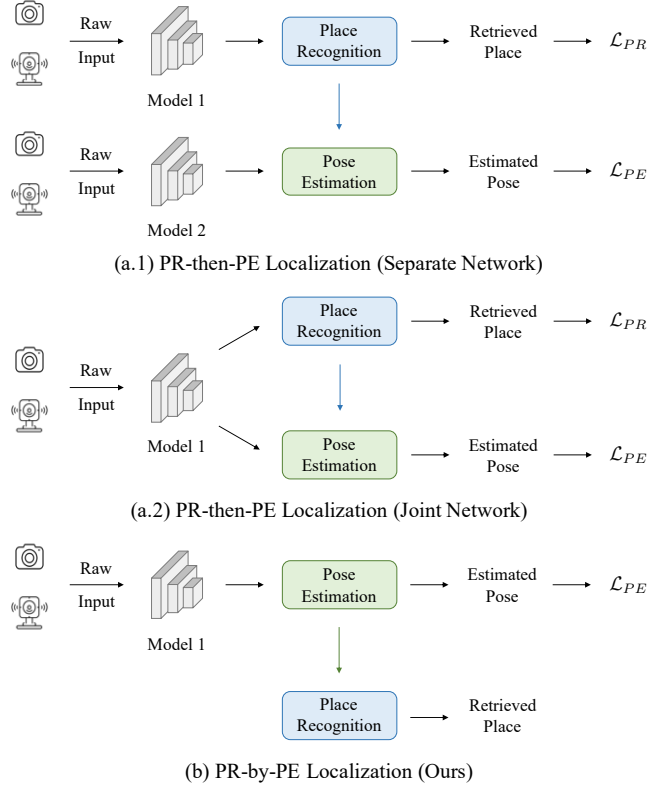


Fig. 1. **Comparison on the various paradigms of global localization.** (a) The PR-then-PE localization paradigm treats place recognition and pose estimation as upstream and downstream tasks, either handled by two independent models (a.1) or jointly learned within a single model (a.2). (b) We introduce a novel paradigm: PR-by-PE localization, which leverages pose estimation to derive place recognition in a single model.

space for subsequent pose estimation. Pose estimation [18]–[24] then estimates the metric pose of the robot by aligning the current observation with these candidates. As depicted in Fig. 1(a.1), early methods handle place recognition and pose estimation using separate models trained independently. Recent research [25]–[31] has advanced this paradigm by integrating place recognition and pose estimation into a single network, leveraging a shared encoder and task-specific heads, as shown in Fig. 1(a.2). Although this integration can reduce computational costs, the common challenge of these *PR-then-PE localization* methods is the heavy rely on the success of place recognition.

Delving into the relationship between place recognition and pose estimation in the *PR-then-PE localization* paradigm, the fundamental issue is the conflicting requirements for place recognition and pose estimation. Place recognition aims for viewpoint invariance, while pose estimation requires viewpoint

<sup>1</sup>Institute of Cyber-Systems and Control, Zhejiang University, China.

<sup>2</sup>School of Astronautics, Beihang University, China.

<sup>3</sup>College of Intelligence Science and Technology, National University of Defense Technology, China.

†Corresponding author: Yue Wang. (E-mail: wangyue@iipc.zju.edu.cn)

awareness. This inherent misalignment causes the inconsistency between the success of pose estimation and place recognition. Pose estimation must fail when place recognition fails, and may still fail even if place recognition succeeds, therefore limiting the whole pipeline performance. At this point, we raise a compelling question: *Can we address global localization by deriving place recognition from pose estimation while maintaining computational efficiency?*

Towards this question, we propose a novel paradigm: *PR-by-PE localization* as shown in Fig. 1(b). A straightforward implementation of this paradigm is to exhaustively apply an off-the-shelf pose solver to compute the relative pose and similarity score (e.g. the number of inliers) of the current observation against all keyframes in the map. The keyframe with the highest similarity score is then selected as the place recognition result. However, these solvers, either require robust optimization [32]–[36] or iterative search [22], which are computationally expensive and prone to local minima. While directly regressing the relative pose between the current observation and all map keyframes offers a faster alternative, it suffers from limited accuracy and lacks a similarity mechanism for place recognition. As for absolute pose regression, it struggles to generalize to unseen environments. Consequently, existing methods are not well-suited for *PR-by-PE localization*. We argue that an effective *PR-by-PE localization* approach requires a relative pose estimation network that is both globally convergent and computationally efficient, with a built-in mechanism for assessing similarity.

To this end, we propose RING#, an end-to-end *PR-by-PE localization* framework that explicitly predicts a 3-DoF pose ( $x$ ,  $y$ , yaw) and a similarity score, supervised solely by the pose estimation loss. The key design is the two equivariant representations to decouple pose estimation into sequential rotation and translation estimation, which effectively reduces the search space dimensionality. By employing a correlation-based exhaustive search on equivariant features in two subspaces, RING# achieves globally convergent pose estimation. The resulting correlation values serve as similarity scores for place recognition, thus effectively embodying the *PR-by-PE localization* paradigm. Thanks to fast correlation computation using the Fast Fourier Transform (FFT), batch processing on GPU, as well as the sparse map keyframe aided by the large convergence basin, RING# is computationally feasible. Additionally, since the core representations in RING# are derived in the bird’s eye view (BEV) space, our framework supports both vision and LiDAR modalities. Overall, our contributions are summarized as follows:

- We introduce a novel paradigm for global localization: *PR-by-PE localization*, which derives place recognition by pose estimation.
- We present RING#, an end-to-end framework that learns equivariant representations to enable globally convergent localization and efficient evaluation.
- We design a BEV-based feature learning architecture that supports both vision and LiDAR modalities.
- We validate the effectiveness of RING# through extensive experiments on the NCLT and Oxford datasets, demonstrating superior performance across both vision and

LiDAR modalities, with RING#-V even outperforming most LiDAR-based methods.

In our previous work RING++ [37], we propose a learning-free framework that aims to construct a roto-translation invariant representation for global localization on a sparse scan map. However, RING++ is limited by its inability to learn from data, leading to suboptimal performance in challenging scenarios and restricting its application to LiDAR inputs only. In contrast, RING# introduces an end-to-end network that learns BEV features while maintaining equivariance to both rotation and translation. This design not only enhances LiDAR-based localization performance, but also extends its applicability to vision-based scenarios. In addition, RING++ operates under the *PR-then-PE localization* paradigm, where errors in place recognition propagate and affect the final pose estimation. RING#, however, adopts the *PR-by-PE localization* paradigm, avoiding the cascading error accumulation. This shift results in a substantial improvement in localization performance, increasing the global localization success rate by nearly 20%.

## II. RELATED WORK

In this section, we provide an overview of methods for visual- and LiDAR-based global localization, followed by a review of methods for BEV representation learning.

**Vision-based Global Localization.** Vision-based localization methods typically adhere to the *PR-then-PE localization* paradigm: place recognition then pose estimation. In the place recognition stage, the most similar map image to the query image is retrieved for coarse localization. Traditional methods rely on handcrafted local features like SIFT [38], SURF [39] and ORB [40] to extract local descriptors, which are then aggregated into global descriptors using aggregation algorithms such as Bag of Words (BoW) [8], Fisher Kernel [41], [42], and Vector of Locally Aggregated Descriptors (VLAD) [7]. With the advent of deep learning, there is a shift towards learned local features [35], [43]–[45], along with learnable aggregation algorithms [9], [46], [47]. In addition to CNN-based methods [10], [11], [13], [15], recent approaches [12], [48], [49] introduce vision Transformers for end-to-end learning of global descriptors. In the pose estimation stage, feature matching methods [33], [34], [36] establish correspondences between query and retrieved images using the above local descriptors. Based on the correspondences, a robust pose solver [18]–[21] is applied to obtain the query pose in the map coordinate. To boost the place recognition performance, matching local features in the above process is employed for the top N candidates, serving as a post-processing step to refine the place recognition result. Recently, there’s a trend towards integrating place recognition and pose estimation in an end-to-end manner [25], [26] or utilizing local matching to re-rank place recognition results [11], [48]–[51].

**LiDAR-based Global Localization.** LiDAR-based localization methods have gained increasing attention due to their robustness to appearance changes. Following the *PR-then-PE localization* paradigm, these methods address global localization through place recognition algorithms, followed by point cloud registration techniques like Iterative Closest Point

(ICP) [22]. M2DP [14] represents 3D point clouds as fingerprints by projecting onto multiple 2D planes. Scan Context and its variants [52]–[56] transform the raw 3D point cloud to a BEV representation in the polar coordinate with the height, intensity, or semantic information. RING [57] and its extension RING++ [37] employ the Radon transform to represent a point cloud as a sinogram for both place recognition and pose estimation. BoW3D [58] exploits a novel linear keypoint descriptor [59] to build BoW for point clouds and achieve LiDAR-based place recognition and pose estimation. Equipped with the power of deep learning, PointNetVLAD [15] extracts local features of a LiDAR scan with PointNet [60] and utilizes NetVLAD [9] to aggregate them into a global descriptor. DiSCO [29] leverages the property of the Fourier transform to output a rotation-invariant global descriptor. OverlapNet [28] and its derivative OverlapTransformer [16] estimate the overlap between two scans for place recognition. DeepRING [17] extracts features from the sinogram to obtain a rotation-invariant global representation. Moreover, SpectralGV [61] presents a spectral method for geometric verification to enhance place recognition performance. Except for learning merely place recognition, some works [27], [30], [31] learn both global and local descriptors for place recognition and pose estimation in a single forward pass.

**BEV Representation Learning.** There are two mainstream classes of view transformation methods to generate BEV features: depth-based methods and transformer-based methods. After LSS [62] method arises, BEV representation is widely used in 3D perception tasks, *e.g.* 3D objection detection, segmentation, and scene completion. These two approaches represent two lines of BEV perception studies. One line of work incorporates depth-based methods like LSS [62], BEVDet [63], BEVDepth [64], *etc.* Depth-based methods lift 2D perspective view (PV) features to 3D features by estimating the depth distribution of each pixel and then generating BEV features by reducing the vertical dimension. The other line is composed of transformer-based methods like DETR3D [65], PETR [66], BEVFormer [67], [68], *etc.* Unlike depth-based methods in a bottom-up manner, transformer-based methods utilize BEV queries to retrieve PV features through the cross-attention mechanism in a top-down manner.

However, the performance of these localization methods is inherently tied to the success of place recognition. When place recognition fails, the overall localization performance suffers significantly. To overcome this limitation, we present a BEV-based *PR-by-PE localization* framework by efficient exhaustive pose estimation, showcasing superior performance.

### III. OVERVIEW

We first introduce the problem statement of global localization in Sec. III-A. Then, we provide an overview of the proposed framework RING# in Sec. III-B.

#### A. Problem Statement

Given a query observation  $Q$  and a database of map keyframe observations  $\mathfrak{M} \triangleq \{M_1, M_2, \dots, M_n\}$  with known poses, the goal of global localization is to estimate the pose

of  $Q$  in the map coordinate. For efficient computation and low memory usage, it is desirable for the density of the map, denoted as  $|\mathfrak{M}|$ , to be as small as possible. In autonomous driving and robotics applications, the gravity direction is easily known and changes in pitch, roll, and height within a local area are generally negligible [69], [70], which reduces the global localization problem from estimating a 6-DoF pose to a 3-DoF pose  $T \in \text{SE}(2)$ . Therefore, we define the global localization problem as a global 3-DoF pose estimation task.  $T$  can be decomposed into a 1-DoF rotation  $\theta \in [0, 2\pi)$  and a 2-DoF translation  $(x, y) \in \mathbb{R}^2$  as follows:

$$T = \begin{bmatrix} \cos \theta & -\sin \theta & x \\ \sin \theta & \cos \theta & y \\ 0 & 0 & 1 \end{bmatrix}. \quad (1)$$

**PR-then-PE Localization.** Existing global localization methods generally adhere to the *PR-then-PE localization* paradigm, formulating the global localization problem as two sequential sub-problems: place recognition and pose estimation. These methods tackle place recognition and pose estimation either using two standalone models or a single model with a shared encoder and task-specific heads to save computational resources. The place recognition algorithm retrieves the most similar map keyframe to  $Q$  from  $\mathfrak{M}$ , as depicted in Eq. (2). Subsequently, the pose estimation algorithm estimates the relative pose between  $Q$  and the retrieved map keyframe, as formulated in Eq. (3).

$$\hat{M}_i = \underset{M_i \in \mathfrak{M}}{\operatorname{argmax}} \mathcal{S}_{pr}(Q, M_i), \quad (2)$$

$$\hat{T}_Q^{\hat{M}_i} = \underset{T_Q^{\hat{M}_i}}{\operatorname{argmax}} \mathcal{S}_{pe}(Q, \hat{M}_i, T_Q^{\hat{M}_i}), \quad (3)$$

where  $\hat{M}_i$  is the retrieved map keyframe,  $\mathcal{S}_{pr}(\cdot)$  is the place recognition similarity function,  $\hat{T}_Q^{\hat{M}_i}$  is the estimated relative pose between  $Q$  and  $\hat{M}_i$ , and  $\mathcal{S}_{pe}(\cdot)$  is the pose estimation similarity function. The global pose of  $Q$  is then derived by

$$\hat{T}_Q^{\mathfrak{M}} = T_{\hat{M}_i}^{\mathfrak{M}} \hat{T}_Q^{\hat{M}_i}, \quad (4)$$

where  $\hat{T}_Q^{\mathfrak{M}}$  is the estimated pose of  $Q$  in the map coordinate, and  $T_{\hat{M}_i}^{\mathfrak{M}}$  is the pose of  $\hat{M}_i$  in the map coordinate. However, the localization performance of such methods heavily depends on the success of place recognition in identifying the most similar map keyframe in the database. If place recognition using  $\mathcal{S}_{pr}(\cdot)$  fails, the output of  $\mathcal{S}_{pe}(\cdot)$  becomes meaningless, inevitably resulting in incorrect localization.

**PR-by-PE Localization.** Rethinking the similarity function in Eq. (3), we note that the map keyframe with the highest similarity after pose alignment should be the correct retrieval for place recognition when performing Eq. (3) for all map keyframes  $M_i$  in  $\mathfrak{M}$ . This insight forms the basis of the *PR-by-PE localization* paradigm. In this paradigm, the 3-DoF localization problem is formulated as

$$\hat{M}_i, \hat{\theta}, \hat{x}, \hat{y} = \underset{M_i \in \mathfrak{M}, \theta, x, y}{\operatorname{argmax}} \mathcal{S}(Q, M_i, \theta, x, y), \quad (5)$$

where  $\hat{M}_i$  is the retrieved map keyframe,  $\hat{\theta}$  is the estimated relative rotation angle,  $(\hat{x}, \hat{y})^T$  is the estimated relative translation vector, and  $\mathcal{S}(\cdot)$  is the *PR-by-PE localization* similarity

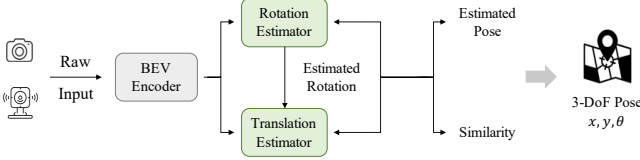


Fig. 2. **PR-by-PE localization framework.** Given a raw sensor observation, we encode it into BEV features first. Based on the BEV features, we construct two equivariant representations that enable the decoupling of pose estimation into rotation estimation and translation estimation.

function. This paradigm derives place recognition as a by-product of pose estimation, effectively bypassing the inherent limitations of *PR-then-PE localization*. However, there are two main challenges in designing an effective similarity function  $S(\cdot)$ : the *efficient evaluation* of similarity across the entire database for each frame, and the *global estimation* of 3-DoF pose to eliminate the dependency on the initial value.

### B. Framework

To address the above challenges, we propose a framework that adopts the *PR-by-PE localization* paradigm, as illustrated in Fig. 2. We first encode sensor observations into BEV features. Based on the BEV features, we construct a rotation-equivariant and translation-invariant representation and a translation-equivariant and rotation-invariant representation (proved in Sec. IV). With these two equivariant representations, we decouple the 3-DoF pose estimation into sequential 1-DoF rotation estimation and 2-DoF translation estimation, thereby reducing the search space dimensionality. For both rotation and translation estimation, we design a correlation-based similarity function to exhaustively search for all possible pose configurations in the 3-DoF pose space. As a result, our localization framework offers the following benefits:

**Built-in Similarity.** The similarity score for place recognition is derived directly from the maximum correlation value obtained through correlation-based pose estimation. This design naturally embodies the *PR-by-PE localization* paradigm, facilitating place recognition by pose estimation.

**Global Convergence.** The construction of equivariant representations ensures that the learned features remain equivariant to pose transformations of the input data. This property enables exhaustive matching between the query and all map keyframes in the database across all possible pose configurations,  $(x, y, \theta)$ . Benefiting from exhaustive matching, our approach converges to the optimal solution without dependency on the initial value.

**Evaluation Efficiency.** The decoupling of 3-DoF pose estimation into rotation and translation estimation, combined with the use of correlation-based similarity function, greatly enhances computational efficiency. This similarity function is accelerated using the Fast Fourier Transform (FFT) and batch processing on GPU, drastically reducing the computational cost. This design enables efficient similarity evaluation across the entire database for each frame, making the exhaustive search feasible in practice.

**Vision and LiDAR Compatibility.** Our framework incorporates a BEV-based feature learning architecture capable of encoding sensor observations into BEV features for both vision

and LiDAR modalities. These BEV features are then used to construct equivariant representations that are effective across different sensor types, allowing the framework applicable to both vision- and LiDAR-based localization.

## IV. EQUIVARIANT REPRESENTATIONS

In this section, we analyze the rotation and translation equivariance and invariance properties of the convolution (CNN), the Radon transform (RT), and the Fourier transform (FT). Upon these properties, we construct two equivariant representations for RING# and provide theoretical proofs.

### A. Definitions

We first present the definition of equivariance and invariance as follows:

**Definition 1** (Equivariance). *For a group of transformations  $G$ , a function  $f$  is equivariant if:*

$$f(T_g[x]) = S_g[f(x)], \quad \forall x \in X, g \in G, \quad (6)$$

where  $x$  is the input,  $g$  is an element of the group  $G$ , and  $T_g$  and  $S_g$  are transformations parameterized by  $g$ .

**Definition 2** (Invariance). *For a group of transformations  $G$ , a function  $f$  is invariant if:*

$$f(T_g[x]) = f(x), \quad \forall x \in X, g \in G, \quad (7)$$

where  $x$  is the input,  $g$  is an element of the group  $G$ , and  $T_g$  is a transformation parameterized by  $g$ .

### B. Convolution

The convolution on  $f(x)$  with the kernel  $h(x)$  is formulated as follows:

$$f_h(x) \triangleq \phi_h(f(x)) = \int_{-\infty}^{\infty} f(u)h(x-u) du, \quad (8)$$

where  $f_h(x)$  is the output of  $f(x)$  after convolution, and  $\phi_h(\cdot)$  is the convolution operator with kernel  $h(x)$ . Then we show the equivariance of the function after applying convolution.

**Lemma 1.**  $\phi_h(f(x))$  is translation equivariant.

*Proof.* Translate the input function  $f(x)$  by  $\Delta x$ , which generates  $f'(x) \triangleq f(x - \Delta x)$ . The convolution on  $f'(x)$  with the kernel  $h(x)$ , denoted as  $f'_h(x)$  is calculated by

$$\begin{aligned} f'_h(x) &= \int_{-\infty}^{\infty} f'(u)h(x-u) du \\ &= \int_{-\infty}^{\infty} f(u-\Delta x)h(x-u) du. \end{aligned} \quad (9)$$

Let  $u' = u - \Delta x$ , which implies  $du' = du$ . Then we have

$$\begin{aligned} f'_h(x) &= \phi_h(f(x - \Delta x)) \\ &= \int_{-\infty}^{\infty} f(u')h((x - \Delta x) - u') du' \\ &= f_h(x - \Delta x). \end{aligned} \quad (10)$$

Therefore,  $\phi_h(f(x))$  is translation equivariant according to Definition 1. In addition, the equivariance can be extended to higher dimensions. We omit the proof here.  $\square$

### C. Radon Transform

The Radon transform [71] is a linear integral transform that computes the integral along a set of straight lines. The mathematical equation of the Radon transform is as follows:

$$\begin{aligned} S(\theta, \tau) &\triangleq \mathcal{R}(f(x, y)) \\ &= \int_{L(\theta, \tau): x \cos \theta + y \sin \theta = \tau} f(x, y) dx dy \\ &= \int_{-\infty}^{\infty} \int_{-\infty}^{\infty} f(x, y) \delta(\tau - x \cos \theta - y \sin \theta) dx dy, \end{aligned} \quad (11)$$

where  $S(\theta, \tau)$  represents the resultant sinogram,  $\mathcal{R}(\cdot)$  denotes the Radon transform operation,  $f(x, y)$  is the input 2D function,  $L(\theta, \tau) : x \cos \theta + y \sin \theta = \tau$  is the line for integral,  $\theta \in [0, 2\pi)$  is the tangent angle of the line  $L(\theta, \tau)$ ,  $\tau \in (-\infty, \infty)$  is the distance from the origin to  $L(\theta, \tau)$ , and  $\delta(\cdot)$  is the Dirac delta function.

**Sinogram after Rotation and Translation.** Let  $f'(x, y)$  be transformed by  $f(x, y)$  with a 3-DoF pose transformation  $T$  parameterized by a rotation angle  $\alpha$  and a translation vector  $t \triangleq (\Delta x, \Delta y)^T$ .  $f'(x, y)$  is formulated as

$$\begin{aligned} f'(x, y) &\triangleq f(R_\alpha X - t), \\ R_\alpha &\triangleq \begin{bmatrix} \cos \alpha & -\sin \alpha \\ \sin \alpha & \cos \alpha \end{bmatrix}, X \triangleq \begin{bmatrix} x \\ y \end{bmatrix}, \end{aligned} \quad (12)$$

where  $R_\alpha$  represents the rotation matrix parameterized by  $\alpha$ .

Applying the Radon transform to  $f'(x, y)$ , the resultant sinogram  $S'(\theta, \tau)$  can be expressed as

$$\begin{aligned} S'(\theta, \tau) &= \mathcal{R}(f'(x, y)) \\ &= \int_{-\infty}^{\infty} \int_{-\infty}^{\infty} f(R_\alpha X - t) \delta(\tau - k_\theta \cdot X) dx dy \\ &= S(\theta + \alpha, \tau - \Delta\tau), \end{aligned} \quad (13)$$

where  $k_\theta \triangleq (\cos \theta, \sin \theta)^T$  is a unit vector of the line  $L(\theta, \tau)$ , and  $\Delta\tau$  is equivalent to the projection of the translation vector  $t$  on the line  $L(\theta + \alpha, \tau)$ , which is calculated by

$$\begin{aligned} \Delta\tau &= k_{\theta+\alpha} \cdot t \\ &= (\cos(\theta + \alpha), \sin(\theta + \alpha)) \cdot (\Delta x, \Delta y) \\ &= \Delta x \cos(\theta + \alpha) + \Delta y \sin(\theta + \alpha). \end{aligned} \quad (14)$$

Therefore, a rotation angle  $\alpha$  on  $f(x, y)$  causes a circular shift along the  $\theta$  axis of  $S(\theta, \tau)$ , and a translation vector  $t$  on  $f(x, y)$  results in a shift in the variable  $\tau$  equal to the projection of  $t$  onto the line  $L(\theta + \alpha, \tau)$ .

**Comparison with Polar Transform.** The polar transform (PT) [72] is widely used to construct an observation representation, which is formulated as

$$\begin{aligned} p(r, \theta) &\triangleq \mathcal{P}(f(x, y)) = f(r \cos \theta, r \sin \theta), \\ r &= \sqrt{x^2 + y^2}, \\ \theta &= \arctan \frac{y}{x}, \end{aligned} \quad (15)$$

where  $p(r, \theta)$  is the result of the polar transform,  $\mathcal{P}(\cdot)$  is the polar transform operator, and  $f(x, y)$  is the input 2D image. The polar transform of  $f'(x, y)$  is formulated as

$$\begin{aligned} p'(r, \theta) &= p(r', \theta'), \\ r' &= \sqrt{(r \cos(\theta + \alpha) - \Delta x)^2 + (r \sin(\theta + \alpha) - \Delta y)^2}, \\ \theta' &= \arctan \frac{r \sin(\theta + \alpha) - \Delta y}{r \cos(\theta + \alpha) - \Delta x}, \end{aligned} \quad (16)$$

where  $p'(r, \theta)$  is the polar representation of  $f'(x, y)$ . In contrast to the Radon transform in Eq. (13), the  $\theta$  axis of  $p(r, \theta)$  is a nonlinear combination of the rotation angle  $\alpha$  and the translation  $t$ , so is the  $r$  axis. Such representation obviously loses equivariance after neural network processing.

### D. Fourier Transform

The Fourier transform [73] is an integral transform that represents a function in the frequency domain, whose formula is

$$\hat{f}(\omega) \triangleq \mathcal{F}(f(x)) = \int_{-\infty}^{\infty} f(x) e^{-i\omega x} dx, \quad (17)$$

where  $f(x)$  is a function in the time domain,  $\mathcal{F}(\cdot)$  is the Fourier transform operator,  $\omega$  is the angular frequency, and  $\hat{f}(\omega)$  is the representation in the frequency domain. Let  $\mathcal{A}(\cdot) \triangleq |\mathcal{F}(\cdot)|$  be the composed operator of  $\mathcal{F}(\cdot)$  and  $|\cdot|$ , where  $|\cdot|$  is the operation of taking magnitude.

**Lemma 2.**  $\mathcal{A}(f(x))$  is translation invariant.

*Proof.* Suppose  $f'(x) \triangleq f(x - \Delta x)$  is the function after translating  $f(x)$  by  $\Delta x$ . Referring to the time shifting property, the Fourier transform converts a shift  $\Delta x$  in the time domain to a phase shift  $-\omega\Delta x$  in the frequency domain:

$$\begin{aligned} \hat{f}'(\omega) &= \mathcal{F}(f(x - \Delta x)) \\ &= \int_{-\infty}^{\infty} f(x - \Delta x) e^{-i\omega x} dx \\ &= \int_{-\infty}^{\infty} f(x - \Delta x) e^{-i\omega(x - \Delta x)} e^{-i\omega\Delta x} d(x - \Delta x) \\ &= e^{-i\omega\Delta x} \int_{-\infty}^{\infty} f(x - \Delta x) e^{-i\omega(x - \Delta x)} d(x - \Delta x) \\ &= e^{-i\omega\Delta x} \hat{f}(\omega). \end{aligned} \quad (18)$$

$\hat{f}'(\omega)$  is the representation of  $f'(x)$  in the frequency domain.

The amplitude of  $\hat{f}'(\omega)$  remains the same regardless of the value of  $\Delta x$ :

$$\begin{aligned} A'(\omega) &= \mathcal{A}(f(x - \Delta x)) \\ &= |\hat{f}'(\omega)| \\ &= |e^{-i\omega\Delta x} \hat{f}(\omega)| \\ &= |\hat{f}(\omega)| \\ &= A(\omega), \end{aligned} \quad (19)$$

where  $A(\omega)$  and  $A'(\omega)$  are the amplitudes of  $f(x)$  and  $f'(x)$  in the frequency domain, satisfying Definition 2. Therefore,  $\mathcal{A}(f(x))$  is translation invariant.  $\square$

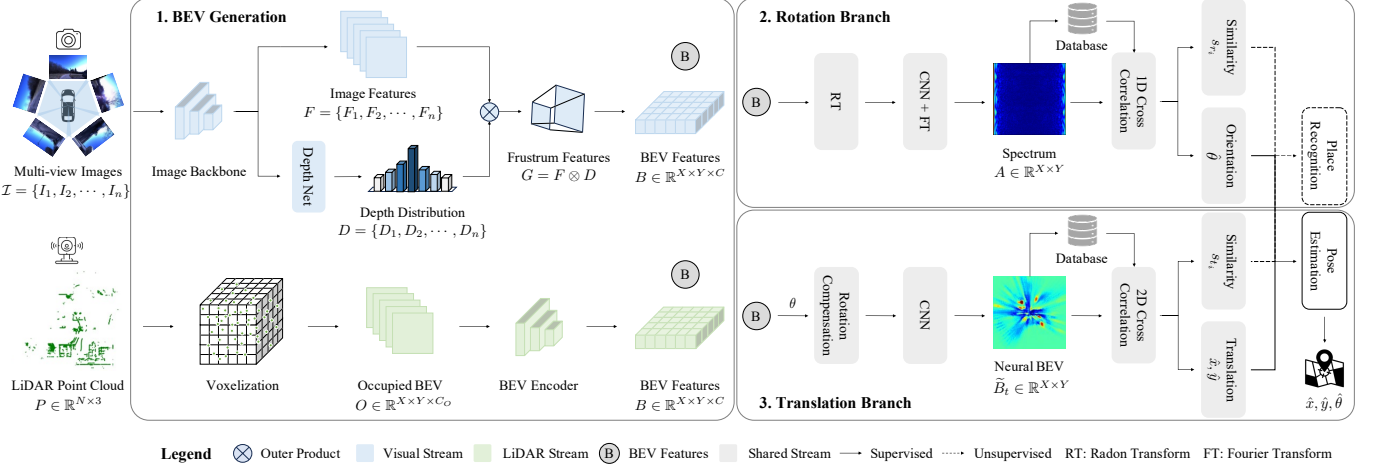


Fig. 3. **Overview of the PR-by-PE localization framework RING#.** 1. Our BEV generation module converts inputs from multi-view images  $\mathcal{I}$  or a LiDAR point cloud  $P$  into BEV features  $B$ . 2. Using the Radon Transform (RT), a Convolutional Neural Network (CNN), and the Fourier Transform (FT), the rotation branch transforms  $B$  into rotation-equivariant and translation-invariant representations  $A$  and then uses 1D cross-correlation to estimate the relative rotation  $\hat{\theta}$ . 3. The translation branch compensates for the relative rotation  $\theta$  which equals to the ground truth rotation  $\theta^*$  during training and equals to the estimated rotation by the rotation  $\hat{\theta}$  branch during inference and uses a CNN to yield rotation-invariant and translation-equivariant representations  $\tilde{B}_t$ . Subsequent 2D cross-correlation is employed to determine the relative translation  $\hat{x}, \hat{y}$ . RING# is supervised by poses only in an end-to-end manner.

#### E. Rotation Equivariant Representation

Given a bounded 2D function  $f(x, y)$ , we first apply the Radon transform  $\mathcal{R}(\cdot)$  to it to generate a sinogram  $S(\theta, \tau)$ . Then, we perform a 1D CNN  $\phi_h(\cdot)$  on the  $\theta$  coordinate of  $S(\theta, \tau)$  to extract features  $S_h(\theta, \tau)$ . Ultimately, we employ the Fourier transform with the magnitude operation  $\mathcal{A}(\cdot)$  to the variable  $\tau$ , yielding the magnitude spectrum  $A(\theta, \omega)$  (i.e. the spectrum in Fig. 3 and Sec. V-B).

**Theorem 1.**  $A(\theta, \omega)$  is rotation equivariant and translation invariant.

*Proof.* By the properties of the RT in Eq. (13), CNN (Lemma 1), and FT (Lemma 2), the magnitude spectrum of  $f'(x, y)$  can be expressed as

$$\begin{aligned} A'(\theta, \omega) &= \mathcal{A}(\phi_h(\mathcal{R}(f'(x, y)))) \\ &= \mathcal{A}(\phi_h(S(\theta + \alpha, \tau - \Delta\tau))) \\ &= \mathcal{A}(S_h(\theta + \alpha, \tau - \Delta\tau)) \\ &= A(\theta + \alpha, \omega), \end{aligned} \quad (20)$$

where  $A'(\theta, \omega)$  is the resultant spectrum generated by  $f'(x, y)$ . The rotation equivariance satisfies Definition 1 and the translation invariance satisfies Definition 2. Therefore,  $A(\theta, \omega)$  is rotation equivariant and translation invariant.  $\square$

#### F. Translation Equivariant Representation

Define  $r(f(x, y), f'(x, y))$  as a function that compensates for the relative rotation between  $f(x, y)$  and  $f'(x, y)$ . The rotation-compensated function,  $\tilde{f}(x, y)$ , is expressed as

$$\tilde{f}(x, y) \triangleq r(f(x, y), f'(x, y)) = f(R_\alpha X), \quad (21)$$

where  $\alpha$  is the rotation angle required to align  $f(x, y)$  with  $f'(x, y)$ , and  $R_\alpha$  is the corresponding rotation matrix.

Given a bounded 2D function  $f(x, y)$ , we use the rotation compensation function  $r(\cdot, \cdot)$  to get a rotation-compensated function  $\tilde{f}(x, y)$ . Then we apply a 2D CNN  $\phi_h(\cdot)$  to  $\tilde{f}(x, y)$ ,

generating features  $\tilde{f}_h(x, y)$  (i.e. the neural BEV in Fig. 3 and Sec. V-C).

**Theorem 2.**  $\tilde{f}_h(x, y)$  is rotation invariant and translation equivariant.

*Proof.* After rotation compensation on  $f(x, y)$  and  $f'(x, y)$ , we have

$$\begin{aligned} \tilde{f}(x, y) &= r(f(x, y), f'(x, y)) \\ &= f(R_\alpha X), \end{aligned} \quad (22)$$

$$\begin{aligned} \tilde{f}'(x, y) &= r(f'(x, y), f'(x, y)) \\ &= f'(x, y), \end{aligned} \quad (23)$$

where  $\tilde{f}'(x, y)$  denotes the rotation compensation of  $f'(x, y)$ . Applying the 2D CNN  $\phi_h(\cdot)$  to  $\tilde{f}(x, y)$ , we can get

$$\begin{aligned} \tilde{f}_h(x, y) &= \phi_h(\tilde{f}(x, y)) = \phi_h(f(R_\alpha X)) \\ &= \phi_h(f(\tilde{x}, \tilde{y})) \\ &= f_h(\tilde{x}, \tilde{y}), \end{aligned} \quad (24)$$

where  $(\tilde{x}, \tilde{y})^T \triangleq R_\alpha X$ . Employing the 2D CNN  $\phi_h(\cdot)$  to  $f'(x, y) = f(R_\alpha X - t)$  and utilizing the translation equivariance of CNN (Lemma 1), we arrive at

$$\begin{aligned} \tilde{f}'_h(x, y) &= \phi_h(\tilde{f}'(x, y)) = \phi_h(f'(x, y)) \\ &= \phi_h(f(R_\alpha X - t)) \\ &= \phi_h(f(\tilde{x} - \Delta x, \tilde{y} - \Delta y)) \\ &= f_h(\tilde{x} - \Delta x, \tilde{y} - \Delta y). \end{aligned} \quad (25)$$

Compared with Eq. (24),  $\tilde{f}_h(x, y)$  is rotation invariant and translation equivariant from Definition 1 and Definition 2.  $\square$

## V. PR-BY-PE LOCALIZATION

In this section, we detail each component of the RING# architecture illustrated in Fig. 3 in the following subsections.

### A. BEV Generation

BEV generation involves distinct two pipelines: one for extracting vision BEV features and the other for deriving LiDAR BEV features.

1) *Vision Stream*: For vision inputs, we adopt the view transformation module in BEVDepth [64] to aggregate multi-view image features from the perspective view into BEV features. It has three sub-modules: a feature extraction module, a depth distribution prediction module, and a feature aggregation module.

**Feature Extraction.** Given a set of multi-view images  $\mathcal{I} = \{I_1, I_2, \dots, I_n\}$  where  $I_i \in \mathbb{R}^{3 \times H \times W}$  is the image captured by the  $i$ th camera,  $n$  is the number of views, we leverage ResNet-50 [74] as the feature extractor  $f_e(\cdot)$  to encode image features  $F = \{F_1, F_2, \dots, F_n\}$ , where  $F_i = f_e(I_i) \in \mathbb{R}^{C_F \times H_F \times W_F}$ ,  $C_F$  is the number of channels,  $H_F$  and  $W_F$  are the height and width of the feature map.

**Depth Distribution Prediction.** To lift 2D features into 3D space, we need to predict the depth distribution of the scene. We input the camera intrinsics and extrinsics into the convolutional neural network DepthNet  $f_d(\cdot)$  in BEVDepth [64] to predict the depth distribution  $D = \{D_1, D_2, \dots, D_n\}$ , where  $D_i = f_d(F_i) \in \mathbb{R}^{C_D \times H_F \times W_F}$ ,  $C_D$  is the number of depth bins. The depth distribution  $D$  is then normalized to  $[0, 1]$  by a sigmoid function. The depth distribution prediction module is trained by minimizing Binary Cross Entropy (BCE) loss.

$$\mathcal{L}_{d_i} = -\frac{1}{N} \sum_{j=1}^{H_F} \sum_{k=1}^{W_F} (D_{ijk}^* \log(D_{ijk}) + (1 - D_{ijk}^*) \log(1 - D_{ijk})), \quad (26)$$

where  $\mathcal{L}_{d_i}$  is the depth loss of the  $i$ th camera image,  $N = H_F \times W_F$  is the total number of pixels, and  $D_i$  and  $D_i^*$  are the predicted and ground truth depth distributions of the  $i$ th camera image.  $D_i^*$  is generated by projecting the 3D LiDAR points onto the  $i$ th camera image. Then the total depth loss is  $\mathcal{L}_d = \sum_{i=1}^n \mathcal{L}_{d_i}$ .

**Feature Aggregation.** Based on the depth distribution  $D$ , we lift the image features  $F$  in the 2D space into frustum features  $G$  in the 3D space:

$$G_i(u, v) = F_i(u, v) \otimes D_i(u, v), \quad (27)$$

where  $G_i(u, v) \in \mathbb{R}^{C_F \times C_D}$  is the output matrix at the feature pixel  $(u, v)$  of the  $i$ th camera image,  $\otimes$  is the outer product operation. To refine the frustum features  $G$ , we apply some  $3 \times 3$  convolution layers for depth refinement. After that, we convert frustum features  $G$  to 3D voxel features  $V \in \mathbb{R}^{X \times Y \times Z \times C}$ . Finally, we use efficient voxel pooling to reduce the vertical dimension  $Z$  and obtain BEV features  $B \in \mathbb{R}^{X \times Y \times C}$ . Through depth supervision and view transformation, the scale of BEV features  $B$  is almost consistent, so we can assume that  $B$  maintains a high degree of equivariance.

2) *LiDAR Stream*: For LiDAR inputs, we directly convert a 3D LiDAR point cloud into a multi-channel BEV representation with occupancy information. Based on the BEV representation, we extract equivariant BEV features using e2cnn [75] detailed below.

**Multi-channel Occupied BEV.** Given a 3D LiDAR point cloud  $P \in \mathbb{R}^{N \times 3}$ , we first remove the ground plane by the  $z$

axis and voxelize it into 3D voxels. Then we assign either 0 (free) or 1 (occupied) to each voxel according to its occupancy, generating a multi-channel occupied BEV  $O \in \mathbb{R}^{X \times Y \times C_O}$ , where  $X$ ,  $Y$ , and  $C_O$  are the number of voxels in the  $x$ ,  $y$ , and  $z$  axis, respectively.

**Equivariant Feature Extraction.** We apply e2cnn [75] to generate equivariant BEV features  $B \in \mathbb{R}^{X \times Y \times C}$  from the multi-channel BEV  $O$ . The e2cnn is a group equivariant convolutional neural network, which is equivariant to the group of 2D Euclidean transformations, namely the E(2) group. The forward pass of e2cnn can be formulated as follows:

$$B = E(O). \quad (28)$$

$E(\cdot)$  is the e2cnn operation,  $O$  is the multi-channel occupied BEV, and  $B \in \mathbb{R}^{X \times Y \times C}$  is the resultant BEV features that are equivariant to discrete SE(2) transformations.

### B. Rotation Branch

The rotation branch comprises a rotation-equivariant representation module and a rotation estimation module. The former transforms BEV features  $B$  into a rotation-equivariant and translation-invariant representation  $A \in \mathbb{R}^{X \times Y}$ . The latter determines the relative rotation between the query and the map keyframe via 1D circular cross-correlation applied to  $A$ .

1) *Rotation Equivariant Representation*: Based on the equivariant BEV features  $B$  developed by the BEV generation module, we employ the Radon transform to each channel of BEV features  $B$  independently to construct a rotation-equivariant sinogram  $S \in \mathbb{R}^{X \times Y \times C}$ . The Radon transform converts a rotation angle on  $B$  into a circular shift on  $S$  in the Radon space, as illustrated in Eq. (13). Then we apply 1D convolutional layers  $\phi_r(\cdot)$  to  $S$  along the  $\theta$  dimension, squeezing the feature channel from  $C$  to 1 and generating features  $S_r \in \mathbb{R}^{X \times Y}$ . To eliminate the effect of large translations, we deploy the Fourier transform along the  $\tau$  axis of  $S_r$  and take the magnitude, yielding the rotation-equivariant and translation-invariant representation  $A$  according to Theorem 1:

$$A(\theta, \omega) = \mathcal{A}(\phi_r(\mathcal{R}(B(x, y, c)))). \quad (29)$$

For general convolutional neural networks, there is a nonlinear activation function like ReLU between convolutions. As such operation is pixel-wise in the feature, the equivariance is still reserved.

2) *Rotation Estimation*: Taking advantage of the rotation equivariance and translation invariance of  $A$ , we solve the relative rotation  $\theta$  between the query  $Q$  and the map keyframe  $M_i$  by 1D circular cross-correlation. The 1D cross-correlation can be formulated as follows:

$$\begin{aligned} c_{r_i}(d_\theta) &= \mathcal{S}_r(A_Q, A_{M_i}, d_\theta) \\ &= A_Q(\theta, \omega) \star A_{M_i}(\theta, \omega) \\ &= \sum_{\theta} \sum_{\omega} A_Q(\theta, \omega) A_{M_i}(\theta - d_\theta, \omega), \end{aligned} \quad (30)$$

where  $c_{r_i}(d_\theta)$  is the resultant correlation vector parameterized by  $d_\theta$ ,  $\mathcal{S}_r(\cdot)$  is the similarity function in the rotation branch,  $A_Q$  and  $A_{M_i}$  are the rotation-equivariant and translation-invariant representations of  $Q$  and  $M_i$ , respectively, and  $\star$  is

the cross-correlation operation. As a result, we can calculate the similarity and the relative rotation angle simultaneously by

$$s_{r_i} = \max_{d_\theta} c_{r_i}(d_\theta), \quad \hat{\theta} = \operatorname{argmax}_{d_\theta} c_{r_i}(d_\theta), \quad (31)$$

where  $s_{r_i}$  and  $\hat{\theta}$  are the similarity and estimated rotation angle, respectively. Due to the property of the Radon transform,  $c_{r_i}(d_\theta)$  is a binomial distribution peaking at  $\hat{\theta}$  and  $\hat{\theta} - \pi$ . Therefore, we choose Kullback-Leibler (KL) divergence loss as the rotation estimation loss:

$$\begin{aligned} q(d_\theta) &= \operatorname{softmax}(c_{r_i}(d_\theta)), \\ \mathcal{L}_r &= \sum_{d_\theta} p(d_\theta) \log \frac{p(d_\theta)}{q(d_\theta)}, \end{aligned} \quad (32)$$

where  $q(d_\theta)$  and  $p(d_\theta)$  are the predicted and ground truth rotation probability distributions.  $p(d_\theta)$  is a binomial gaussian distribution peaking at  $\theta^*$  (ground truth rotation) and  $\theta^* - \pi$ .

### C. Translation Branch

To eliminate the rotation effect, we employ the function specified in Eq. (21) to the BEV features of  $Q$  and  $M_i$ , which rotates the BEV features of  $Q$  by an angle  $\theta$ , defined as:

$$\theta = \begin{cases} \theta^*, & \text{in the training phase} \\ \hat{\theta}, & \text{in the inference phase.} \end{cases} \quad (33)$$

After rotation compensation, we apply 2D convolution layers  $\phi_t(\cdot)$  to the rotation-compensated BEV features  $\tilde{B}$ , resulting in the rotation-invariant and translation-equivariant neural BEV  $\tilde{B}_t \in \mathbb{R}^{X \times Y}$  as stated in Theorem 2.  $\tilde{B}_{t_Q}$  and  $\tilde{B}_{t_{M_i}}$  of  $Q$  and  $M_i$  are generated by

$$\tilde{B}_{t_Q} = \phi_t(B_Q(R_\theta X)), \quad \tilde{B}_{t_{M_i}} = \phi_t(B_{M_i}), \quad (34)$$

where  $\theta$  is defined as in Eq. (33), and  $R_\theta$  is the associated rotation matrix. Subsequently, to determine the relative translation between  $Q$  and  $M_i$ , we employ 2D cross-correlation:

$$\begin{aligned} c_{t_i}(d_x, d_y) &= \mathcal{S}_t(\tilde{B}_{t_Q}, \tilde{B}_{t_{M_i}}, d_x, d_y) \\ &= \tilde{B}_{t_Q}(x, y) \star \tilde{B}_{t_{M_i}}(x, y) \\ &= \sum_x \sum_y \tilde{B}_{t_Q}(x, y) \tilde{B}_{t_{M_i}}(x - d_x, y - d_y), \end{aligned} \quad (35)$$

where  $c_{t_i}(d_x, d_y)$  is the 2D correlation map and  $\mathcal{S}_t(\cdot)$  is the similarity function in the translation branch. Then the similarity  $s_{t_i}$  and relative translation  $\hat{x}, \hat{y}$  can be estimated simultaneously by

$$s_{t_i} = \max_{d_x, d_y} c_{t_i}(d_x, d_y), \quad \hat{x}, \hat{y} = \operatorname{argmax}_{d_x, d_y} c_{t_i}(d_x, d_y). \quad (36)$$

We choose negative log-likelihood (NLL) loss as the translation estimation loss:

$$\begin{aligned} q(d_x, d_y) &= \operatorname{softmax}(c_{t_i}(d_x, d_y)), \\ \mathcal{L}_t &= -\log(q(x^*, y^*)), \end{aligned} \quad (37)$$

where  $q(d_x, d_y)$  is the predicted translation probability and  $(x^*, y^*)^T$  is the ground truth translation vector. The total loss is  $\mathcal{L} = \lambda_d \mathcal{L}_d + \lambda_r \mathcal{L}_r + \lambda_t \mathcal{L}_t$ , where  $\lambda_d$ ,  $\lambda_r$ , and  $\lambda_t$  are the weights of the depth, rotation, and translation losses.

### D. Place Recognition Derived by Pose Estimation

In a *PR-by-PE* localization manner, place recognition is a by-product of pose estimation in our method. By Eq. (31) and Eq. (36), we can estimate the similarity  $s_{r_i}$  and  $s_{t_i}$  between the query  $Q$  and each map keyframe  $M_i$  in the database  $\mathfrak{M}$ , which enables place recognition. We select  $\mathcal{S}_t(\cdot)$  in Eq. (35) as the similarity function to recognize places.

$$\begin{aligned} \hat{M}_i, \hat{x}, \hat{y} &= \operatorname{argmax}_{M_i \in \mathfrak{M}, d_x, d_y} \mathcal{S}_t(\tilde{B}_{t_Q}, \tilde{B}_{t_{M_i}}, d_x, d_y) \\ &= \operatorname{argmax}_{M_i \in \mathfrak{M}, d_x, d_y} \mathcal{S}_t(\phi_t(B_Q(R_\theta X)), \phi_t(B_{M_i}), d_x, d_y), \\ \text{s.t. } \hat{\theta} &= \operatorname{argmax}_{d_\theta} c_{r_i}(d_\theta). \end{aligned} \quad (38)$$

Finally, we re-write this similarity function as

$$\hat{M}_i, \hat{\theta}, \hat{x}, \hat{y} = \operatorname{argmax}_{M_i \in \mathfrak{M}, d_\theta, d_x, d_y} \mathcal{S}(B_Q, B_{M_i}, d_\theta, d_x, d_y), \quad (39)$$

which can be regarded as a concrete form of Eq. (5). This form allows for rotation and translation estimation by correlation-based exhaustive search, making the solver to Eq. (39) global and efficient, satisfying the desirable properties.

### E. Pose Refinement

Upon the estimated pose  $\hat{\theta}, \hat{x}, \hat{y}$ , we perform additional pose refinement to yield a more accurate pose. In the vision stream, we employ 3-DoF exhaustive matching on the neural BEV in a local range to refine the pose. Specifically, we rotate the query BEV features  $B_Q$  by a set of candidate angles  $\Theta = \{\theta_1, \theta_2, \dots, \theta_m\}$  as inputs of  $\phi_t(\cdot)$ , generating  $\{\tilde{B}_{t_{Q_1}}, \tilde{B}_{t_{Q_2}}, \dots, \tilde{B}_{t_{Q_m}}\}$ . Referring to Eq. (35) and Eq. (36), the refined pose is computed by

$$\begin{aligned} \hat{\theta}, \hat{x}, \hat{y} &= \operatorname{argmax}_{\theta_j \in \Theta, d_x, d_y} \mathcal{S}_t(\tilde{B}_{t_{Q_j}}, \tilde{B}_{t_{M_i}}, d_x, d_y) \\ &= \operatorname{argmax}_{\theta_j \in \Theta, d_x, d_y} \mathcal{S}_t(\phi_t(B_Q(R_{\theta_j} X)), \phi_t(B_{M_i}), d_x, d_y), \end{aligned} \quad (40)$$

where  $R_{\theta_j}$  is the rotation matrix of  $\theta_j$  and  $\hat{M}_i$  is the retrieved map keyframe by Eq. (39). In the LiDAR stream, we refine the 3-DoF pose by ICP alignment with FastGICP [76]. Ultimately, we obtain the localization pose of query  $Q$  against map coordinate by Eq. (4).

## VI. EXPERIMENTS

In this section, we evaluate our method on the NCLT and Oxford datasets (Sec. VI-A) in terms of place recognition (Sec. VI-D), pose estimation (Sec. VI-E), two-stage global localization evaluation (Sec. VI-F) and one-stage global localization evaluation (Sec. VI-G) under three evaluation protocols (Sec. VI-C), respectively. Moreover, we carry out ablation studies (Sec. VI-H) to further investigate the effectiveness of the proposed method. Finally, we compare the runtime of our approach with other approaches (Sec. VI-I).

### A. Datasets

**NCLT Dataset** [77] is a long-term dataset collected by a mobile segway robot in an urban environment. It contains 27 sessions with environmental changes, including weather, illumination, and season changes. The ground truth 6DoF poses are provided by a high-precision RTK GPS system. It contains loops under various rotation changes, which is widely used in the field of global localization. It provides six-view camera images captured by Pointgrey Ladybug3 omnidirectional camera and 3D scans collected by Velodyne HDL-32E. In our experiments, we use five-view camera images as inputs to train RING#-V since the camera 0 faces the sky, which is useless for localization. Besides, we also crop the images and resize them to  $224 \times 384$  to save the training memory.

**Oxford Radar RobotCar Dataset** [78] is a large-scale dataset collected by a mobile car mounted on multi-view cameras, LiDAR (Velodyne HDL-32E) and Radar (FMCW) sensors, which is a radar extension of the Oxford Robotcar dataset [79]. It covers a large area of Oxford city center and contains multiple sessions with environmental changes in January 2019. The car is equipped with one Point Grey Bumblebee XB3 trinocular camera and three Point Grey Grasshopper2 monocular cameras for  $360^\circ$  vision sensing. Additionally, it utilizes two Velodyne HDL-32E mounted on the left and right of the radar for 3D scene understanding. In our experiments, we leverage four-view camera images captured from the center stereo camera of Point Grey Bumblebee XB3 and three Point Grey Grasshopper2 monocular cameras to train the vision model. Likewise, we crop these images and resize them to  $320 \times 640$  during image preprocessing. In the LiDAR stream, we concatenate the point clouds collected by the left and right 3D LiDAR sensors into a single point cloud for training and evaluation. Since the ground truth poses of the Oxford dataset are not enough precise, we apply FastGICP [76] for ICP refinement to generate more accurate poses.

### B. Implementation Details

We implement our method in PyTorch [80] and train it on two NVIDIA GeForce RTX 4090 GPUs. We use the Adam optimizer [81] with a learning rate of  $1 \times 10^{-3}$  and a weight decay of  $1 \times 10^{-4}$ . We follow the batch size strategy in [82] for batch generation, setting our batch size to 16. The loss weights  $\lambda_d$ ,  $\lambda_r$ , and  $\lambda_t$  are set to 3.0, 1.0 and 1.0. We exclusively rely on pose supervision, training our model with data collected within a 25m radius of the current pose for 30 epochs.

For vision-based BEV generation, we adopt the method in BEVDepth [64] to construct the BEV features  $B \in \mathbb{R}^{128 \times 128 \times 80}$ . The BEV features  $B$  represent the spatial range of  $[102.4m \times 102.4m]$  with a grid size of  $0.8m$ . In the LiDAR stream, the multi-channel occupied BEV  $O \in \mathbb{R}^{160 \times 160 \times 20}$  and the extracted BEV features  $B \in \mathbb{R}^{160 \times 160 \times 128}$  both represent a region of  $[140m \times 140m]$  with a grid size of  $0.875m$ . Regarding the RING#-V model, we first train our model on depth estimation and then the whole model based on the pre-trained model. We train models on the NCLT and Oxford datasets separately.

### C. Evaluation Protocols

We propose three protocols to evaluate compared methods under three different variations: place variation, appearance variation, and both place and appearance variation.

- **Protocol 1: Place Variation.** We evaluate the performance of compared methods under place variation. We split the sessions into training and test sets. Then, we train the model on the split training set and evaluate it on the split test set. The test sessions are collected in the same season and weather conditions as the training sessions. For the NCLT dataset, we choose “2012-02-04” as the map session and “2012-03-17” as the query session, and then follow [17] to split the training and test sets. For the Oxford dataset, we split “2019-01-11-13-24-51” and “2019-01-15-13-06-37” sessions into training and test sets for training and evaluation respectively.
- **Protocol 2: Appearance Variation.** We evaluate the performance of compared methods under appearance variation. We train the model on several entire sessions and test it on other entire sessions that are not included in the training sessions. The test sessions are collected in different seasons and weather conditions. For the NCLT dataset, we select “2012-02-04”, “2012-03-17”, “2012-05-26”, and “2013-04-05” sequences for training and “2012-01-08”, “2012-08-20” and “2012-11-16” sequences for testing. For the Oxford dataset, we select the entire sequence of “2019-01-11-13-24-51” as the map session and the entire sequence of “2019-01-15-13-06-37” as the query session for training. In the test phase, “2019-01-11-14-37-14” is used as the map session, and “2019-01-17-12-48-25” is used as the query session.
- **Protocol 3: Place and Appearance Variation.** We evaluate the performance of compared methods under both place and appearance variation. We utilize the trained model in Protocol 1 to evaluate the performance on the test sessions in Protocol 2. Specifically, we test all methods on “2012-01-08”, “2012-08-20”, and “2012-11-16” sequences of Protocol 2 using the model trained on the split “2012-02-04” and “2012-03-17” sequences of Protocol 1 for the NCLT dataset. Likewise, we test all methods on “2019-01-11-14-37-14” and “2019-01-17-12-48-25” sequences of Protocol 2 using the model trained on the split “2019-01-11-13-24-51” and “2019-01-15-13-06-37” sequences of Protocol 1 for the Oxford dataset.

In the following experiments, we perform multi-session localization evaluation, where the query and map trajectories are sampled at 5m and 20m intervals, as used in [37].

### D. Evaluation of Place Recognition

**Metrics.** For place recognition evaluation, a revisit threshold ( $r$  meters) is used to determine whether a retrieved match is correct. A retrieval is deemed successful if it lies within this threshold from the query. In this experiment, we set the revisit threshold to  $r = 10m$ . We leverage five metrics to quantify the performance of all methods: 1) Recall@1: the percentage of queries whose top 1 retrieved match is correct; 2) F1 Score: the harmonic mean of precision (the ratio of

TABLE I  
QUANTITATIVE RESULTS OF PLACE RECOGNITION OF PROTOCOL 1

Approach	Input	NCLT			Oxford		
		Recall@1 ↑	F1 Score ↑	AUC ↑	Recall@1 ↑	F1 Score ↑	AUC ↑
Vision	Exhaustive SS [33], [43] <sup>†</sup>	M	0.66	0.74	<u>0.82</u>	<b>0.86</b>	<b>0.91</b>
	NetVLAD [9]	P	0.37	0.51	0.43	0.62	0.75
	Patch-NetVLAD [11]	P	0.41	0.54	0.43	0.67	0.78
	AnyLoc [12]	P	0.47	0.60	0.42	0.73	0.83
	SFRS [10]	P	0.50	0.62	0.54	0.74	0.83
	BEV-NetVLAD-MLP	M	0.60	0.71	0.64	0.74	0.83
	vDiSCO [83]	M	<u>0.76</u>	<u>0.82</u>	0.73	<u>0.80</u>	<u>0.87</u>
LiDAR	<b>RING#-V (Ours)</b>	M	<b>0.82</b>	<b>0.86</b>	<b>0.93</b>	<b>0.86</b>	<b>0.91</b>
	OverlapTransformer [16]	L	0.71	0.78	0.76	0.71	0.81
	LCDNet [31]	L	0.70	0.78	0.75	0.62	0.75
	DiSCO [29]	L	0.76	0.82	0.80	0.87	0.91
	RING [57]	L	0.67	0.76	0.79	0.76	0.84
	RING++ [37]	L	0.68	0.77	0.78	0.83	0.89
	EgoNN [30]	L	<u>0.80</u>	<u>0.85</u>	<u>0.85</u>	<u>0.89</u>	<u>0.92</u>
	<b>RING#-L (Ours)</b>	L	<b>0.85</b>	<b>0.87</b>	<b>0.91</b>	<b>0.91</b>	<b>0.93</b>

<sup>†</sup> SS: Superpoint + SuperGlue. M: Multi-view images. P: Panorama images. L: LiDAR point clouds. The best result is highlighted in **bold** and the second best is underlined.

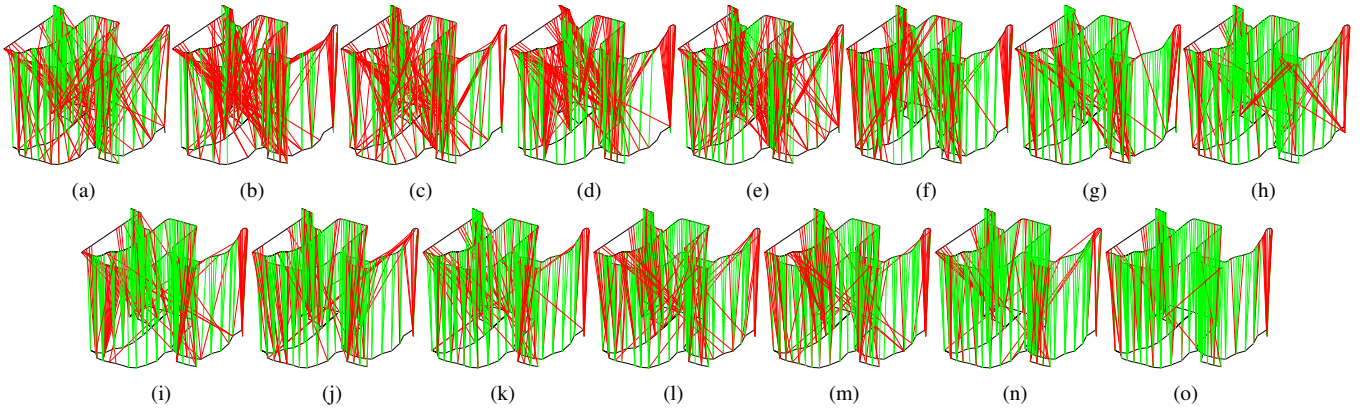


Fig. 4. Top 1 retrieved matches for protocol 1 on the NCLT dataset. (a) Exhaustive SS [33], [43]. (b) NetVLAD [9]. (c) Patch-NetVLAD [11]. (d) AnyLoc [12]. (e) SFRS [10]. (f) BEV-NetVLAD-MLP. (g) vDiSCO [83]. (h) RING#-V (Ours). (i) OverlapTransformer [16]. (j) LCDNet [31]. (k) DiSCO [29]. (l) RING [57]. (m) RING++ [37]. (n) EgoNN [30]. (o) RING#-L (Ours). The black line — represents the trajectory, the green line — represents the correct retrieval match, and the red line — represents the wrong retrieval match.

true positives to retrieved matches) and recall (the ratio of true positives to actual positives) at various thresholds<sup>4</sup>, with the maximum F1 score reported; 3) Precision-Recall Curve: a curve that plots the precision and recall of the retrieval results as the threshold<sup>4</sup> changes; 4) AUC (Area Under Curve): the area under the precision-recall curve to quantitatively evaluate the performance of the precision-recall curve; 5) Recall@N: the ratio of queries where at least one of the top N retrieved matches is correct.

**Baselines.** We evaluate our method against a range of state-of-the-art approaches across vision and LiDAR modalities. In the vision domain, we compare against several image matching and retrieval techniques in the PV space, including Exhaustive SS (SuperPoint [43] + SuperGlue [33]), NetVLAD [9], Patch-NetVLAD [11], AnyLoc [12], and SFRS [10]. Exhaustive SS combines SuperPoint and SuperGlue to exhaustively perform feature matching, selecting the match with the highest number of inliers as the top 1 retrieval. For AnyLoc, we select the ViT-G AnyLoc-VLAD-DINOv2 model that uses

the foundation model DINOv2 [84] for feature extraction. Under a multi-camera setup, these image retrieval methods use panoramic images as inputs for a fair comparison. Additionally, we evaluate BEV-based approaches BEV-NetVLAD-MLP and vDiSCO [83]. BEV-NetVLAD-MLP consists of a shared BEV-based backbone with a NetVLAD head for place recognition and a multi-layer perceptron (MLP) head for pose estimation, where the BEV-based backbone is the same as RING#, providing a direct comparison in the BEV space. In the LiDAR domain, we compare our method with six leading approaches: OverlapTransformer [16], LCDNet [31], DiSCO [29], RING [57], RING++ [37], and EgoNN [30]. Except for Exhaustive SS, AnyLoc, and SFRS, for which we use the authors' pre-trained weights, we retrain all other methods using the official implementations on both datasets.

**Results.** Table I compares the place recognition performance of all methods under Protocol 1. Among the PV-based methods, Exhaustive SS, which follows the *PR-by-PE localization* paradigm, achieves the best performance across all metrics on the NCLT and Oxford datasets. This demonstrates that pose estimation sufficiently improves the performance of

<sup>4</sup>The threshold refers to the similarity threshold for determining whether a match is a positive retrieval.



Fig. 5. Qualitative vision examples of some queries and their top 1 retrieved matches on the NCLT dataset. The red rectangle  $\square$  represents the wrong retrieval result and the green rectangle  $\square$  represents the correct retrieval result.

place recognition, validating the effectiveness of the proposed paradigm. However, Exhaustive SS is computationally expensive and is not an end-to-end localization model. Besides, it suffers from environmental changes, thereby resulting in a decline in performance from the Oxford dataset to the NCLT dataset. On the other hand, BEV-NetVLAD-MLP and vDiSCO leverage the inherent structural awareness of BEV features, achieving competitive performance compared to the PV-based methods. Specifically, vDiSCO’s explicit rotation invariance design makes it surpass BEV-NetVLAD-MLP, particularly on the NCLT dataset that contains more viewpoint changes. While vDiSCO, adhering to *PR-then-PE localization*, surpasses Exhaustive SS on the NCLT dataset, it still lags behind on the Oxford dataset. This confirms the benefits of the *PR-by-PE localization* paradigm. RING# designs an end-to-end *PR-by-PE localization* network in the BEV space, enabling RING#-V to exhibit the best place recognition performance overall. With 3D geometry information, LiDAR-based methods generally outperform vision-based methods. Methods like DiSCO and EgoNN own better rotation invariance design, surpassing OverlapTransformer and LCDNet. Despite lacking learned features, RING and RING++ with explicit rotation invariance design show comparable and even better performance than OverlapTransformer and LCDNet. In contrast, RING#-L explicitly constructs equivariant representations for *PR-by-PE localization*, demonstrating the state-of-the-art performance on both datasets. This finding aligns with the results observed in vision-based methods, where the *PR-by-PE localization* paradigm significantly enhances place recognition performance.

We visualize the top 1 retrieved matches on two distinct trajectories of the NCLT dataset in Fig. 4, which demonstrates the same result as Recall@1. Fig. 5 and Fig. 6 further display some qualitative results of queries and their top 1 retrieved matches. Our approach consistently succeeds under various conditions, such as viewpoint and seasonal changes, where some compared methods fail. The underlying reason is that the explicit equivariance modeling in RING# enables the network to learn patterns invariant to environmental changes while remaining invariant to viewpoint changes. In contrast, compared methods tend to learn patterns that are coupled with changes in environment and viewpoint. Apart from Recall@1, we report the recall of the top 10 retrieved matches on the NCLT and Oxford datasets, which is plotted in Fig. 7. Moreover, we present precision-recall curves of all methods as depicted in Fig. 8. The results illustrate that our method has superior performance in both vision and LiDAR modalities across the NCLT and Oxford datasets, verifying that place recognition derived by exhaustive pose estimation marginally improves the performance. Notably, RING#-V performs better than RING#-L in terms of precision-recall curves since visual data provides richer appearance information than LiDAR data, which enhances place recognition when combined with geometric information from BEV features.

#### E. Evaluation of Pose Estimation

We perform pure pose estimation evaluation under Protocol 1 without the interference of place recognition to compare the pure pose estimation performance. In detail, we estimate the

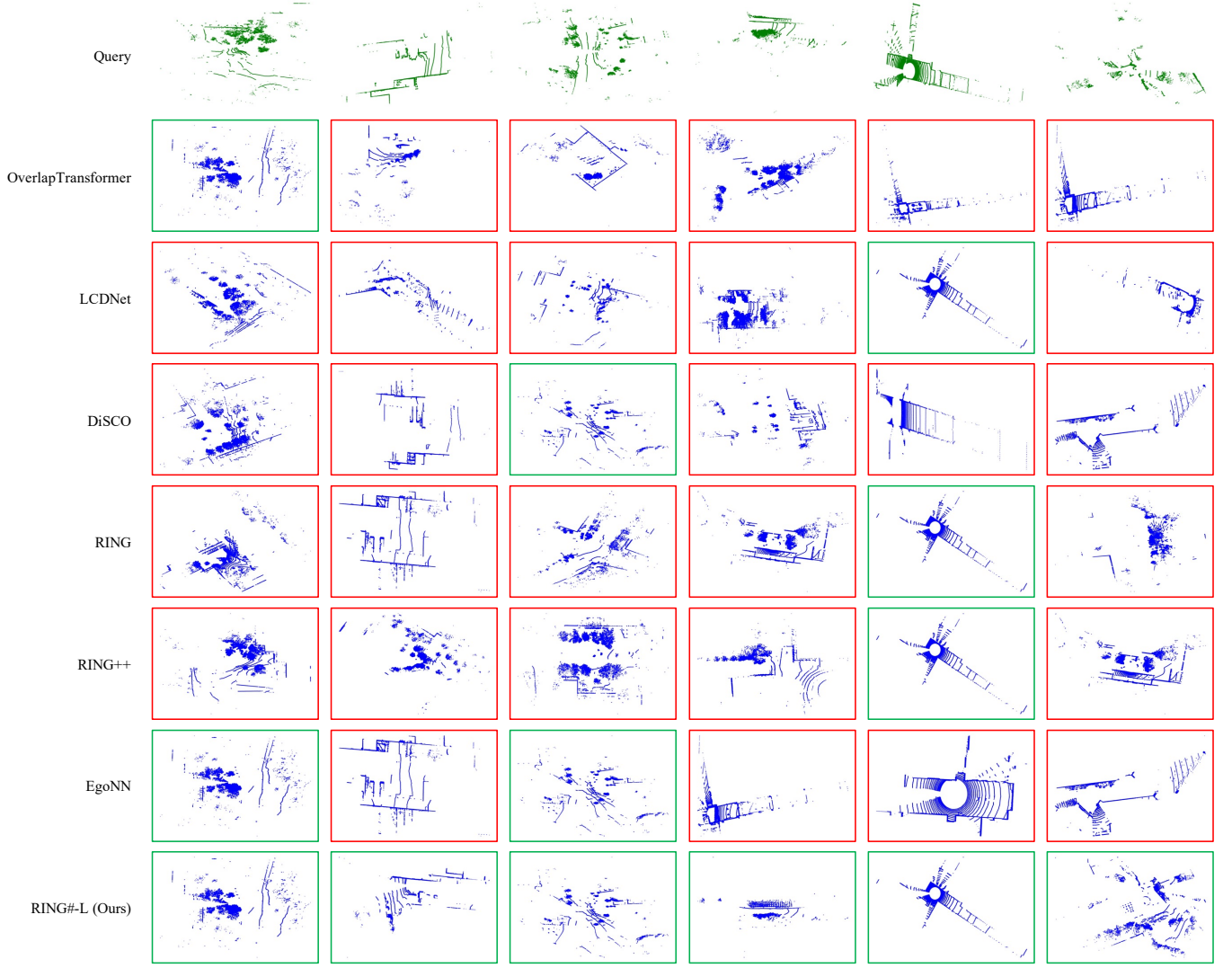


Fig. 6. Qualitative LiDAR examples of some queries and their top 1 retrieved matches on the NCLT dataset. The red rectangle  $\square$  represents the wrong retrieval result and the green rectangle  $\square$  represents the correct retrieval result.

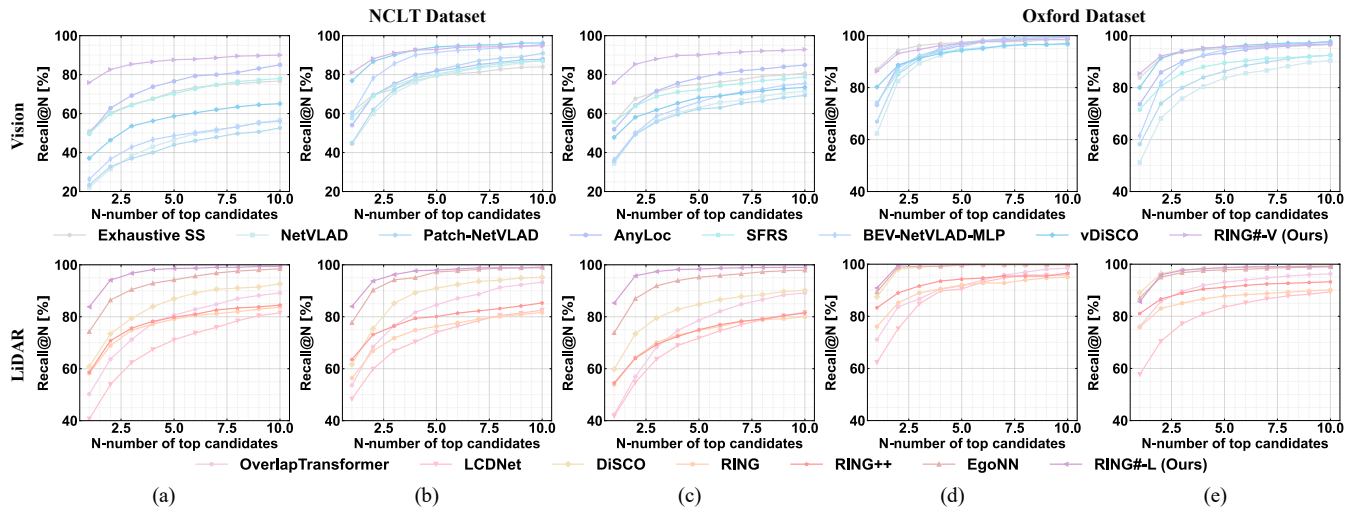


Fig. 7. Recall@N curves on the NCLT and Oxford datasets. (a) 2012-01-08 to 2012-08-20. (b) 2012-01-08 to 2012-11-16. (c) 2012-08-20 to 2012-11-16. (d) 2019-01-11-13-24-51 to 2019-01-15-13-06-37. (e) 2019-01-11-13-24-51 to 2019-01-17-12-48-25.

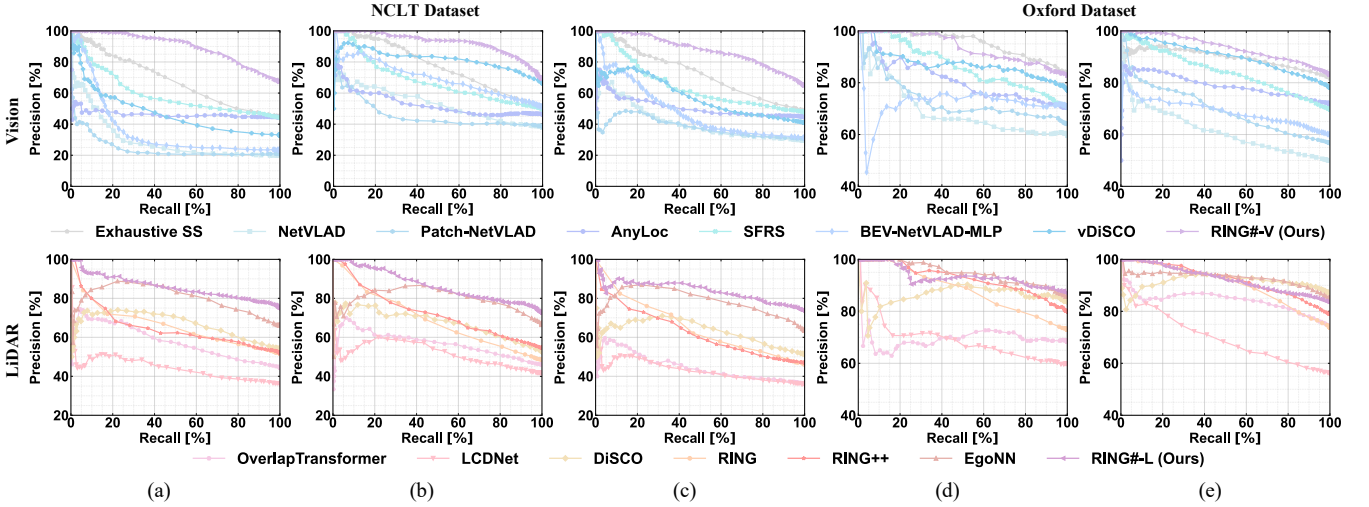


Fig. 8. Precision-recall curves on the NCLT and Oxford datasets. (a) 2012-01-08 to 2012-08-20. (b) 2012-01-08 to 2012-11-16. (c) 2012-08-20 to 2012-11-16. (d) 2019-01-11-13-24-51 to 2019-01-15-13-06-37. (e) 2019-01-11-13-24-51 to 2019-01-17-12-48-25.

relative pose of each query with every reference within a 10m radius in the map trajectory.

**Metrics.** We use three metrics to evaluate the pose estimation performance: 1) RE (Rotation Error), which measures the difference between the estimated and ground truth rotation angle; 2) TE (Translation Error), which measures the difference between the estimated and ground truth translation; 3) PE Succ. (Pose Estimation Success Rate), which calculates the ratio of queries that satisfy  $RE < 5^\circ$  and  $TE < 2m$ . In this paper, we focus on 3-DoF pose errors (1-DoF RE and 2-DoF TE) and report 50th and 75th percentile errors.

**Baselines.** We compare RING#-V with both handcrafted and learning-based local feature matching methods. We evaluate SIFT [38] and SuperPoint [43] feature extractors with the Nearest Neiborhood (NN) and SuperGlue [33] matchers. To perform these methods with multi-view images as inputs, we assign multi-view matched image pairs according to the ground truth rotation angle. We replace detected 2D keypoints on the reference image with 3D keypoints using the ground truth depth projected from the LiDAR point cloud. After that, we filter out the outliers and estimate the pose transformation with PnP [85] + RANSAC [18]. We also assess the pose estimation performance of BEV-NetVLAD-MLP, a BEV-based method that predicts 3-DoF poses. For LiDAR-based methods, we compare RING#-L with the same methods listed in Sec. VI-D followed by ICP refinement using FastGICP [76]. Additionally, for methods that perform both place recognition and pose estimation, we evaluate their pose estimation performance without ICP refinement to provide a comprehensive comparison.

**Results.** We report the pose errors and success rates in Table II. Superpoint + SuperGlue, which integrates learned feature detection and matching, outperforms other vision baselines. However, it is relatively slow during the 2D-3D matching process and generates a large ratio of outliers under large appearance variations. BEV-NetVLAD-MLP, which directly regresses relative 3-DoF poses from BEV features, offers a faster alternative but sacrifices accuracy, resulting in larger pose errors. In contrast, RING#-V demonstrates a significant reduc-

tion in pose errors, particularly at the 75th percentile, reaching the highest PE Succ. on both datasets. This improvement is attributed to the end-to-end learning of equivariant features in the BEV space that allows RING#-V to effectively capture the geometric structure of the environment, which is essential for accurate pose estimation. Among the LiDAR baselines capable of predicting 3-DoF or 6-DoF poses without ICP registration, LCDNet and EgoNN rely on local feature matching and the robust RANSAC estimator for pose estimation. Despite this, they are outperformed by RING and RING++, which employ a globally convergent pose solver. RING#-L further enhances this by introducing learnable equivariant feature extraction, significantly boosting the discriminative power of the features and delivering excellent performance. After ICP alignment, all approaches present better performance. For instance, LCDNet with ICP increases PE Succ. by 43% and 60% on the NCLT and Oxford datasets, respectively. Nevertheless, methods like OverlapTransformer and DiSCO, which either do not estimate relative poses or only predict 1-DoF rotations, fail to provide effective initial poses for ICP, leading to inferior results. This highlights the critical role of accurate pose estimation. Conversely, RING#-L maintains superior PE Succ. with or without ICP, demonstrating its robustness and global convergence capabilities. Furthermore, we provide the qualitative results that visualize the pose estimation process of RING#-V and RING#-L in Fig. 9. As we can see, the neural BEV of RING#-V and RING#-L reveals a pattern consistent with the input LiDAR point cloud, highlighting the strong equivariance and geometric awareness of the neural BEV, which accounts for the superior performance of RING# in pose estimation.

#### F. Two-stage Evaluation of Global Localization

We evaluate global localization performance in two stages under different protocols in Sec. VI-C and revisit thresholds.

**Metrics.** In addition to the evaluation metrics (RE, TE, and PE Succ.) used in Sec. VI-E, we introduce one more metric for global localization evaluation: GL Succ., which is defined as the percentage of queries that are correctly localized ( $RE < 5^\circ$  and  $TE < 2m$ ). For two-stage evaluation of global localization,

TABLE II  
QUANTITATIVE RESULTS OF POSE ESTIMATION OF PROTOCOL 1

Approach	NCLT			Oxford		
	RE [ $^{\circ}$ ] $\downarrow$	TE [m] $\downarrow$	PE Succ. $\uparrow$	RE [ $^{\circ}$ ] $\downarrow$	TE [m] $\downarrow$	PE Succ. $\uparrow$
Vision	SIFT [38] + NN $^{\dagger}$	40.36 / 126.99	8.90 / 23.72	0.11	0.63 / 2.87	0.68 / 3.84
	SuperPoint [43] + NN $^{\dagger}$	24.76 / 171.14	5.12 / 7.84	0.22	0.84 / 4.07	0.85 / 4.50
	SuperPoint [43] + SuperGlue [33] $^{\dagger}$	3.31 / 9.02	2.34 / 5.68	0.43	0.59 / 2.51	0.45 / 2.62
	BEV-NetVLAD-MLP	57.98 / 121.56	5.82 / 8.24	0.01	6.71 / 14.60	6.75 / 12.07
	<b>RING#-V (Ours)</b>	<b>1.25 / 2.22</b>	<b>0.71 / 1.29</b>	<b>0.85</b>	0.76 / 1.48	0.76 / 1.85
LiDAR w/o ICP	LCDNet [31]	3.91 / 9.04	3.47 / 5.65	0.25	3.35 / 8.49	5.11 / 7.91
	RING [57]	1.37 / 2.36	0.56 / <b>0.83</b>	0.88	0.79 / 1.49	0.60 / 1.03
	RING++ [37]	1.30 / 2.28	0.58 / 0.88	0.91	0.78 / 1.41	0.55 / 0.93
	EgoNN [30]	1.57 / 4.43	<b>0.40</b> / 2.02	0.71	<b>0.39 / 0.96</b>	0.56 / 4.78
	<b>RING#-L (Ours)</b>	<b>1.13 / 1.85</b>	0.62 / 0.86	<b>0.97</b>	0.54 / 0.98	<b>0.51 / 0.80</b>
LiDAR w/ ICP	OverlapTransformer [16] + ICP [76]	86.36 / 172.68	4.29 / 8.08	0.31	0.01 / 0.22	0.02 / 5.58
	LCDNet [31] + ICP [76]	1.23 / 2.70	0.22 / 4.05	0.67	<b>0.00 / 0.01</b>	<b>0.00 / 1.19</b>
	DiSCO [29] + ICP [76]	1.14 / 2.16	0.19 / 1.39	0.75	0.01 / 0.06	0.02 / 5.42
	RING [57] + ICP [76]	1.05 / 1.78	<b>0.14</b> / 0.25	0.92	<b>0.00 / 0.01</b>	<b>0.00 / 0.06</b>
	RING++ [37] + ICP [76]	1.03 / 1.77	<b>0.14</b> / 0.23	0.95	<b>0.00 / 0.01</b>	<b>0.00 / 0.01</b>
	EgoNN [30] + ICP [76]	1.15 / 2.32	0.15 / 0.34	0.79	<b>0.00 / 0.02</b>	<b>0.00 / 4.59</b>
	<b>RING#-L (Ours) + ICP [76]</b>	<b>0.99 / 1.68</b>	<b>0.14 / 0.22</b>	<b>0.97</b>	<b>0.00 / 0.00</b>	<b>0.00 / 0.01</b>

$\dagger$  NN: Nearest Neighbor. We report 50th and 75th percentile errors for RE and TE. The best result is highlighted in **bold** and the second best is underlined.

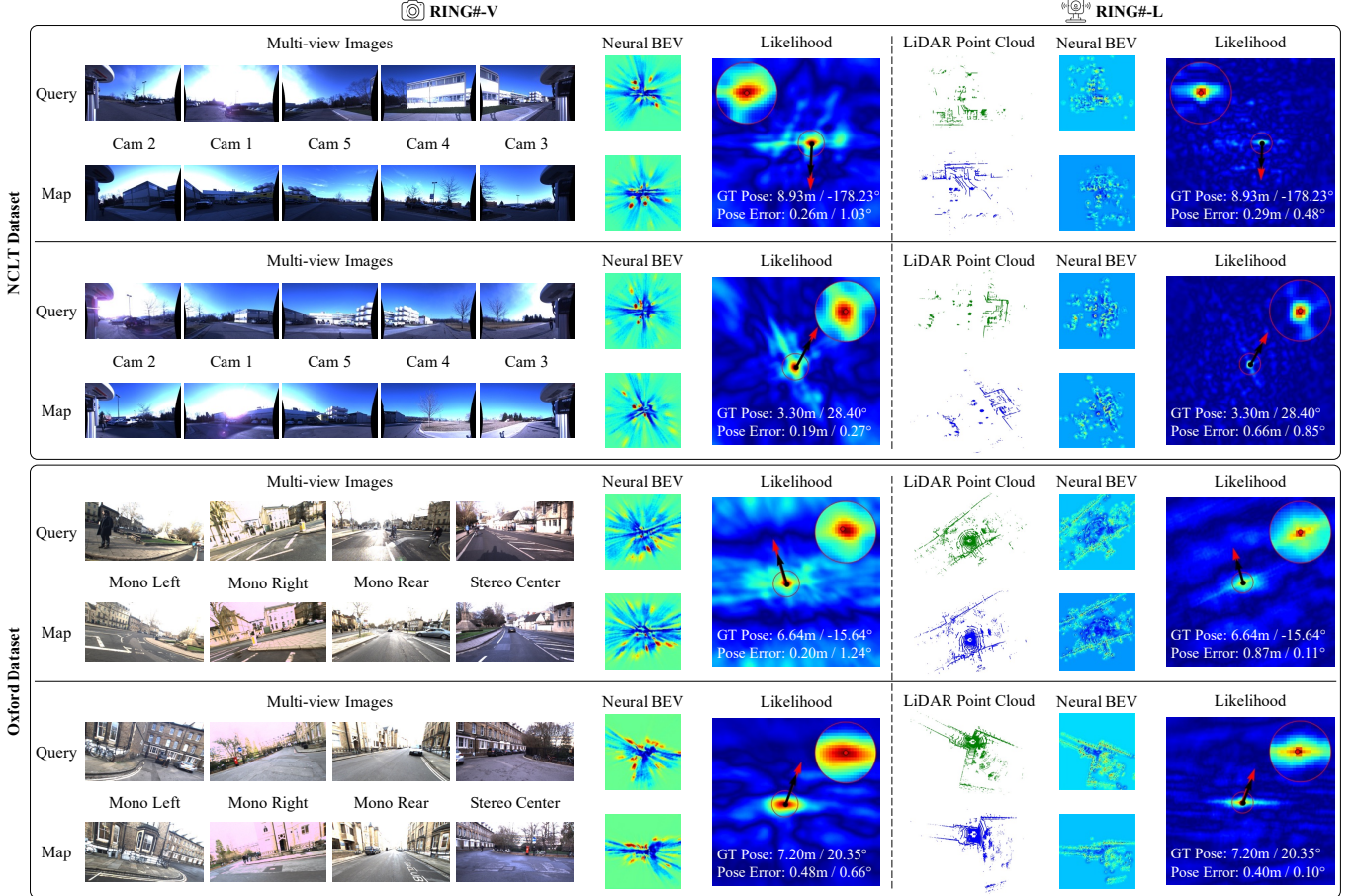


Fig. 9. **Qualitative localization results of RING#-V and RING#-L.** We display several localization cases of RING# on the NCLT and Oxford datasets. On the likelihood plot, the black arrow  $\rightarrow$  shows the pose estimated by RING#, the red arrow  $\rightarrow$  shows the ground truth pose and the red dot  $\bullet$  shows the ground truth position. Here we rotate the query neural BEV by  $\hat{\theta}$  estimated using RING# to visualize the neural BEV under a 3-DoF pose transformation.

GL Succ. is a compound metric of place recognition and pose estimation, formulated as  $GL\text{ Succ.} = \text{Recall}@1 \times PE\text{ Succ.}$ .

**Baselines.** We combine all visual place recognition methods in Sec. VI-D with pose estimation methods SuperPoint + SuperGlue (abbreviated as SS) as the vision baselines. The

LiDAR baselines are composed of LiDAR place recognition methods in Sec. VI-D followed by ICP registration.

**Results under Different Protocols.** A revisit threshold of  $r = 10m$  is used in these experiments. The global localization results using all protocols are presented in Table III to Table V.

In the vision domain, vDiSCO + SS achieves comparable GL Succ. to Exhaustive SS on the NCLT dataset and even slightly surpasses it under Protocol 2. This is attributed to its explicit design of rotation-invariant descriptors in the BEV space. Despite this, Exhaustive SS achieves better overall performance across both datasets, showcasing the advantages of the *PR-by-PE localization* paradigm. As an end-to-end BEV-based *PR-by-PE localization* method, RING#-V consistently outperforms all other methods across various protocols and datasets. In the LiDAR domain, EgoNN, an end-to-end *PR-then-PE localization* network that extracts both global and local descriptors for place recognition and pose estimation, exhibits competitive results among the compared methods. However, RING#-L, specifically designed for *PR-by-PE localization*, generally surpasses EgoNN, except under Protocol 2 on the Oxford dataset, where EgoNN shows a slight edge. The reason for this exception in Protocol 2 will be discussed later. It is worth noting that RING#-V even outperforms most LiDAR-based methods, reinforcing our claim that the *PR-by-PE localization* paradigm is more effective than the *PR-then-PE localization* paradigm.

Exhaustive SS and RING++ serve as reliable indicators of the difficulty level of the evaluation sequences across different protocols, given that they are either not retrained or non-learnable. By comparing their performance across the three protocols, it is evident that the evaluation sequences of Protocol 2 and 3 are more challenging than those of Protocol 1. Notably, Protocol 3 is more challenging than Protocol 2 since it assesses global localization performance using models trained on Protocol 1 but evaluated on the same sequences as Protocol 2. As a result, most approaches exhibit a performance drop from Protocol 1 and 2 to Protocol 3, particularly on the NCLT dataset. In contrast, RING#-V and RING#-L consistently deliver superior performance across all three protocols, demonstrating excellent generalization ability.

**Results under Different Revisit Thresholds.** Interestingly, the performance of RING#-L in Protocol 2, despite benefiting from more training data, is lower than in Protocol 3. This decline is primarily due to a drop in place recognition performance, as indicated by a decrease in Recall@1. We hypothesize the reason is that *the strict revisit threshold of place recognition rejects some potential queries that can be correctly localized*. To verify this hypothesis, we analyze the pose errors at different revisit thresholds (5m, 10m, 20m, 25m) as shown in Fig. 10 to study the impact of revisit thresholds. The results show that the pose errors RE and TE of all baselines increase significantly with higher revisit thresholds. Nonetheless, RING#-V and RING#-L almost maintain nearly constant RE and TE as the revisit threshold increases. This consistent performance suggests that the revisit threshold of  $r = 10m$  used in previous experiments underestimates the true potential of RING#, which could achieve even better performance with a higher revisit threshold.

#### G. One-stage Evaluation of Global Localization

To further confirm the hypothesis, we compare two-stage evaluation (with a strict revisit threshold) and one-stage (without a strict revisit threshold) evaluation of global localization.

**Metrics.** For two-stage evaluation of global localization in Sec. VI-F, GL Succ. = Recall@1  $\times$  PE Succ., where the denominator of PE Succ. is the number of correct retrievals. GL Succ. equals PE Succ. with the denominator being the number of queries for one-stage evaluation of global localization.

**Baselines.** The baselines are the same as that in Sec. VI-F.

**Results.** Fig. 11 reports the global localization success rate under two-stage and one-stage evaluation. We conduct a statistical analysis using the two-tailed Mann-Whitney U test [86] to determine the statistical significance of the proposed method. The results show that GL Succ. of all methods increases from two-stage evaluation to one-stage evaluation without the influence of the revisit threshold. In particular, RING#-V and RING#-L improve GL Succ. by 8.27% and 18.20% in comparison to two-stage evaluation. This further confirms our hypothesis that *GL Succ. is improved by eliminating the strict revisit threshold of place recognition*. Additionally, the Mann-Whitney U test indicates that our method, RING#, outperforms state-of-the-art methods with statistically significant improvements in performance.

#### H. Ablation Study

The impact of different modules in RING# architecture, as well as the impact of different map intervals in evaluation, are explored in the ablation study.

**Equivariance Construction.** Table VI shows the place recognition and pure pose estimation performance of RING#-V with different modules on the NCLT dataset under Protocol 1.  $\mathcal{M}_1$  to  $\mathcal{M}_4$  represent different variants of RING#-V, distinguished by the placement of CNNs in the rotation and translation branches.  $\mathcal{M}_1$ , which omits CNNs in both branches, performs the worst, underscoring the necessity of CNNs for achieving great performance in RING#-V.  $\mathcal{M}_3$  reaches better performance than  $\mathcal{M}_2$ , which confirms the effectiveness of our rotation equivariance construction in the rotation branch, as stated in Theorem 1. Additionally,  $\mathcal{M}_4$  outperforms  $\mathcal{M}_3$  by 20% Recall@1, validating the translation equivariance construction detailed in Theorem 2. These findings underscore the critical importance of a well-designed, learnable equivariance architecture.

**Depth Supervision and Pose Refinement.** We also investigate the effects of depth supervision and pose refinement by comparing  $\mathcal{M}_4$  through  $\mathcal{M}_6$ .  $\mathcal{M}_5$  achieves slightly better Recall@1 and PE Succ. than  $\mathcal{M}_4$  due to the enhanced depth accuracy provided by depth supervision.  $\mathcal{M}_6$ , which follows  $\mathcal{M}_5$ 's architecture but adds 3-DoF exhaustive matching upon the neural BEV in the translation branch for pose refinement, achieves the best performance among all variants. This indicates that rotation estimation noise in the rotation branch can be effectively mitigated by this refinement process.

**Localization Paradigm.** The performance of RING#-V trained under different localization paradigms is assessed by comparing  $\mathcal{M}_6$  to  $\mathcal{M}_8$ .  $\mathcal{M}_7$  is trained solely with the place recognition loss (Cross-Entropy loss) based on the similarity calculated in the rotation branch, focusing exclusively on the place recognition task. The inferior performance of  $\mathcal{M}_7$  indicates that separately training place recognition is less

TABLE III  
QUANTITATIVE RESULTS OF GLOBAL LOCALIZATION OF PROTOCOL 1

Approach	NCLT			Oxford		
	GL / PE Succ. $\uparrow$	RE [ $^\circ$ ] $\downarrow$	TE [m] $\downarrow$	GL / PE Succ. $\uparrow$	RE [ $^\circ$ ] $\downarrow$	TE [m] $\downarrow$
Vision	Exhaustive SS [33], [43] $^\dagger$	0.38 / 0.57	2.71 / 5.32	1.45 / 3.45	0.73 / 0.84	<b>0.34 / 0.89</b> / 0.35 / <b>0.77</b>
	NetVLAD [9] + SS [33], [43] $^\dagger$	0.20 / 0.52	2.92 / 6.79	1.71 / 4.07	0.51 / 0.81	0.38 / 1.16 / 0.37 / 0.93
	Patch-NetVLAD [11] + SS [33], [43] $^\dagger$	0.22 / 0.54	2.63 / 4.92	1.72 / 3.84	0.55 / 0.82	<u>0.35</u> / 1.06 / 0.35 / 0.81
	AnyLoc [12] + SS [33], [43] $^\dagger$	0.28 / 0.59	<u>2.15</u> / 4.95	1.19 / 3.51	0.59 / 0.81	0.36 / 1.36 / <b>0.34</b> / 1.02
	SFRS [10] + SS [33], [43] $^\dagger$	0.30 / <u>0.61</u>	2.57 / <u>4.77</u>	<u>1.08</u> / 3.34	0.61 / 0.82	0.36 / 1.11 / <u>0.35</u> / 0.96
	BEV-NetVLAD-MLP	0.00 / 0.01	61.05 / 121.83	5.16 / 7.48	0.05 / 0.06	5.77 / 10.64 / 7.08 / 11.47
	vDiSCO [83] + SS [33], [43] $^\dagger$	0.38 / 0.50	2.93 / 7.18	1.74 / 4.05	0.66 / 0.82	<u>0.35</u> / 0.90 / 0.36 / 0.78
<b>RING#-V (Ours)</b>		<b>0.75 / 0.91</b>	<b>1.11 / 2.02</b>	<b>0.65 / 1.03</b>	<b>0.78 / 0.90</b>	1.71 / 2.48 / 0.68 / 1.07
LiDAR	OverlapTransformer [16] + ICP [76]	0.27 / 0.38	47.26 / 172.39	3.70 / 7.38	0.48 / 0.68	0.01 / 0.06 / 0.01 / 4.49
	LCDNet [31] + ICP [76]	0.50 / 0.72	1.21 / 1.95	0.17 / 2.81	0.54 / 0.87	<b>0.00</b> / 0.01 / <b>0.00</b> / 0.01
	DiSCO [29] + ICP [76]	0.62 / 0.81	<u>0.97</u> / 1.67	0.15 / 0.35	0.60 / 0.68	0.01 / 0.04 / 0.01 / 4.49
	RING [57] + ICP [76]	0.65 / <u>0.97</u>	0.98 / <u>1.64</u>	0.13 / <u>0.20</u>	0.71 / 0.94	<b>0.00</b> / <b>0.00</b> / <b>0.00</b> / <b>0.00</b>
	RING++ [37] + ICP [76]	0.66 / 0.96	0.98 / <u>1.64</u>	<b>0.12</b> / 0.21	<u>0.81</u> / <u>0.98</u>	<b>0.00</b> / <b>0.00</b> / <b>0.00</b> / <b>0.00</b>
	EgoNN [30] + ICP [76]	0.76 / 0.95	0.98 / 1.68	<b>0.12</b> / 0.21	0.79 / 0.89	<b>0.00</b> / <b>0.00</b> / <b>0.00</b> / <b>0.00</b>
	<b>RING#-L (Ours) + ICP [76]</b>	<b>0.83 / 0.98</b>	<b>0.94 / 1.53</b>	<b>0.12 / 0.18</b>	<b>0.90 / 0.99</b>	<b>0.00</b> / <b>0.00</b> / <b>0.00</b> / <b>0.00</b>

$^\dagger$  SS: SuperPoint + SuperGlue. We report 50th and 75th percentile errors for RE and TE. The best result is highlighted in **bold** and the second best is underlined.

TABLE IV  
QUANTITATIVE RESULTS OF GLOBAL LOCALIZATION OF PROTOCOL 2

Approach	NCLT			Oxford		
	GL / PE Succ. $\uparrow$	RE [ $^\circ$ ] $\downarrow$	TE [m] $\downarrow$	GL / PE Succ. $\uparrow$	RE [ $^\circ$ ] $\downarrow$	TE [m] $\downarrow$
Vision	Exhaustive SS [33], [43] $^\dagger$	0.33 / <u>0.60</u>	<u>2.01</u> / 4.48	<u>1.20</u> / 3.05	<u>0.69</u> / 0.83	0.38 / 1.02 / 0.42 / 1.13
	NetVLAD [9] + SS [33], [43] $^\dagger$	0.20 / 0.43	2.94 / 8.57	2.26 / 5.45	0.39 / 0.75	0.45 / 1.36 / 0.51 / 1.90
	Patch-NetVLAD [11] + SS [33], [43] $^\dagger$	0.21 / 0.44	3.02 / 8.76	2.12 / 5.53	0.37 / 0.74	0.49 / 1.42 / 0.54 / 2.05
	AnyLoc [12] + SS [33], [43] $^\dagger$	0.25 / 0.48	2.61 / 7.23	1.78 / 4.54	0.58 / 0.78	0.44 / 1.20 / 0.46 / 1.54
	SFRS [10] + SS [33], [43] $^\dagger$	0.28 / 0.51	2.36 / 6.55	1.64 / 4.32	0.58 / 0.81	<b>0.37</b> / <b>0.98</b> / <b>0.40</b> / <u>1.12</u>
	BEV-NetVLAD-MLP	0.03 / 0.04	11.56 / 27.42	4.27 / 6.46	0.13 / 0.17	4.99 / 9.50 / 2.93 / 4.72
	vDiSCO [83] + SS [33], [43] $^\dagger$	<u>0.37</u> / 0.43	2.95 / 8.37	2.26 / 5.24	0.62 / 0.79	0.44 / 1.15 / 0.46 / 1.52
<b>RING#-V (Ours)</b>		<b>0.79 / 0.95</b>	<b>1.31 / 2.26</b>	<b>0.73 / 1.02</b>	<b>0.81 / 0.93</b>	0.65 / 1.07 / 0.48 / <b>0.74</b>
LiDAR	OverlapTransformer [16] + ICP [76]	0.30 / 0.43	3.85 / 164.88	2.62 / 7.06	0.57 / 0.72	0.01 / 0.06 / 0.01 / 2.95
	LCDNet [31] + ICP [76]	0.28 / 0.63	1.39 / 3.22	0.22 / 3.82	0.58 / <b>0.93</b>	<b>0.00</b> / <b>0.00</b> / <b>0.00</b> / <b>0.00</b>
	DiSCO [29] + ICP [76]	0.61 / 0.74	1.15 / 2.29	0.21 / 0.85	0.66 / 0.75	0.01 / 0.04 / 0.01 / 2.02
	RING [57] + ICP [76]	0.53 / 0.95	<u>1.09</u> / 2.05	<b>0.15</b> / <b>0.23</b>	0.71 / <b>0.93</b>	<b>0.00</b> / <b>0.00</b> / <b>0.00</b> / <b>0.00</b>
	RING++ [37] + ICP [76]	0.56 / <u>0.96</u>	1.10 / <u>2.03</u>	<b>0.15</b> / 0.24	0.76 / <b>0.93</b>	<b>0.00</b> / <b>0.00</b> / <b>0.00</b> / <b>0.00</b>
	EgoNN [30] + ICP [76]	<u>0.75</u> / 0.89	1.14 / 2.16	0.16 / 0.28	<b>0.81</b> / 0.92	<b>0.00</b> / <b>0.00</b> / <b>0.00</b> / <b>0.00</b>
	<b>RING#-L (Ours) + ICP [76]</b>	<b>0.78 / 0.97</b>	<b>1.07 / 1.98</b>	<b>0.15 / 0.24</b>	<b>0.79 / 0.93</b>	<b>0.00</b> / <b>0.00</b> / <b>0.00</b> / <b>0.00</b>

$^\dagger$  SS: SuperPoint + SuperGlue. We report 50th and 75th percentile errors for RE and TE. The best result is highlighted in **bold** and the second best is underlined.

TABLE V  
QUANTITATIVE RESULTS OF GLOBAL LOCALIZATION OF PROTOCOL 3

Approach	NCLT			Oxford		
	GL / PE Succ. $\uparrow$	RE [ $^\circ$ ] $\downarrow$	TE [m] $\downarrow$	GL / PE Succ. $\uparrow$	RE [ $^\circ$ ] $\downarrow$	TE [m] $\downarrow$
Vision	Exhaustive SS [33], [43] $^\dagger$	<u>0.33</u> / <u>0.60</u>	<u>2.01</u> / 4.48	<u>1.20</u> / 3.05	<u>0.69</u> / 0.83	0.38 / 1.02 / 0.42 / 1.13
	NetVLAD [9] + SS [33], [43] $^\dagger$	0.15 / 0.47	2.78 / 8.08	1.74 / 5.01	0.39 / 0.77	0.45 / 1.22 / 0.46 / 1.75
	Patch-NetVLAD [11] + SS [33], [43] $^\dagger$	0.16 / 0.47	2.75 / 7.64	1.72 / 4.88	0.46 / 0.78	0.42 / 1.14 / 0.46 / 1.40
	AnyLoc [12] + SS [33], [43] $^\dagger$	0.25 / 0.48	2.61 / 7.23	1.78 / 4.54	0.58 / 0.78	0.44 / 1.20 / 0.46 / 1.54
	SFRS [10] + SS [33], [43] $^\dagger$	0.28 / 0.51	2.36 / 6.55	1.64 / 4.32	0.58 / 0.81	<b>0.37</b> / <b>0.98</b> / <b>0.40</b> / <u>1.12</u>
	BEV-NetVLAD-MLP	0.01 / 0.02	22.48 / 60.75	5.21 / 7.23	0.05 / 0.07	6.42 / 10.96 / 4.70 / 7.88
	vDiSCO [83] + SS [33], [43] $^\dagger$	0.25 / 0.47	2.80 / 7.49	1.89 / 4.64	0.62 / 0.78	0.44 / 1.21 / 0.46 / 1.59
<b>RING#-V (Ours)</b>		<b>0.72 / 0.94</b>	<b>1.28 / 2.25</b>	<b>0.61 / 0.91</b>	<b>0.79 / 0.92</b>	0.66 / 1.10 / 0.52 / <b>0.81</b>
LiDAR	OverlapTransformer [16] + ICP [76]	0.22 / 0.45	3.21 / 160.05	2.15 / 6.83	0.56 / 0.73	0.01 / 0.06 / 0.01 / 2.54
	LCDNet [31] + ICP [76]	0.27 / 0.62	1.42 / 3.26	0.21 / 4.07	0.53 / 0.91	<b>0.00</b> / <b>0.00</b> / <b>0.00</b> / 0.01
	DiSCO [29] + ICP [76]	0.44 / 0.73	1.17 / 2.33	0.20 / 2.97	0.67 / 0.75	0.01 / 0.04 / 0.01 / 2.10
	RING [57] + ICP [76]	0.53 / 0.95	<b>1.09</b> / 2.05	<b>0.15</b> / <b>0.23</b>	0.71 / <b>0.93</b>	<b>0.00</b> / <b>0.00</b> / <b>0.00</b> / <b>0.00</b>
	RING++ [37] + ICP [76]	0.56 / <u>0.96</u>	1.10 / <u>2.03</u>	<b>0.15</b> / 0.24	0.76 / <b>0.93</b>	<b>0.00</b> / <b>0.00</b> / <b>0.00</b> / <b>0.00</b>
	EgoNN [30] + ICP [76]	0.67 / 0.89	1.13 / 2.14	0.16 / 0.28	0.79 / 0.91	<b>0.00</b> / <b>0.00</b> / <b>0.00</b> / <b>0.00</b>
	<b>RING#-L (Ours) + ICP [76]</b>	<b>0.82 / 0.97</b>	<b>1.09 / 2.00</b>	<b>0.15 / 0.24</b>	<b>0.80 / 0.93</b>	<b>0.00</b> / <b>0.00</b> / <b>0.00</b> / <b>0.00</b>

$^\dagger$  SS: SuperPoint + SuperGlue. We report 50th and 75th percentile errors for RE and TE. The best result is highlighted in **bold** and the second best is underlined.

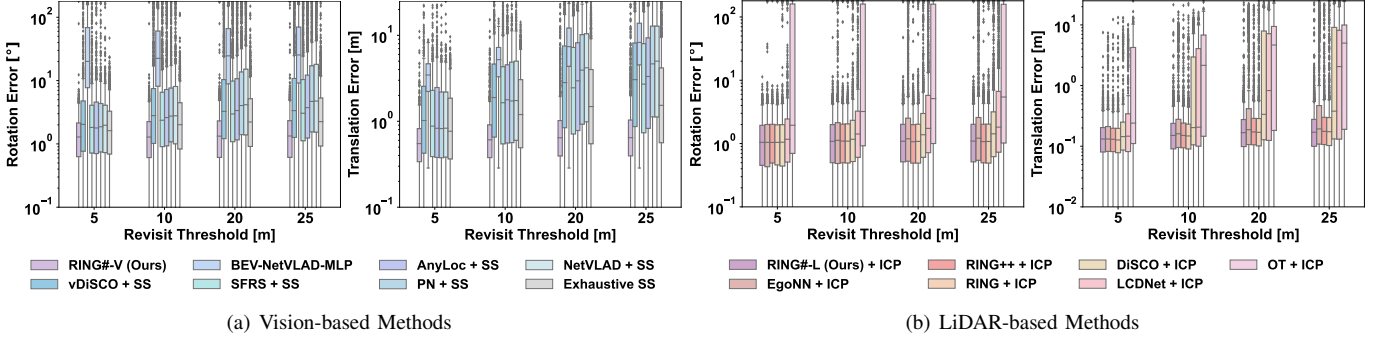


Fig. 10. **Pose errors at different revisit thresholds of the NCLT dataset.** SS: SuperPoint + SuperGlue, PN: Patch-NetVLAD, OT: OverlapTransformer. (a) and (b) present rotation and translation errors of vision-based and LiDAR-based methods at 5m, 10m, and 20m revisit threshold. Compared to other methods, RING#-V and RING#-L show minimal changes in pose errors across different revisit thresholds.

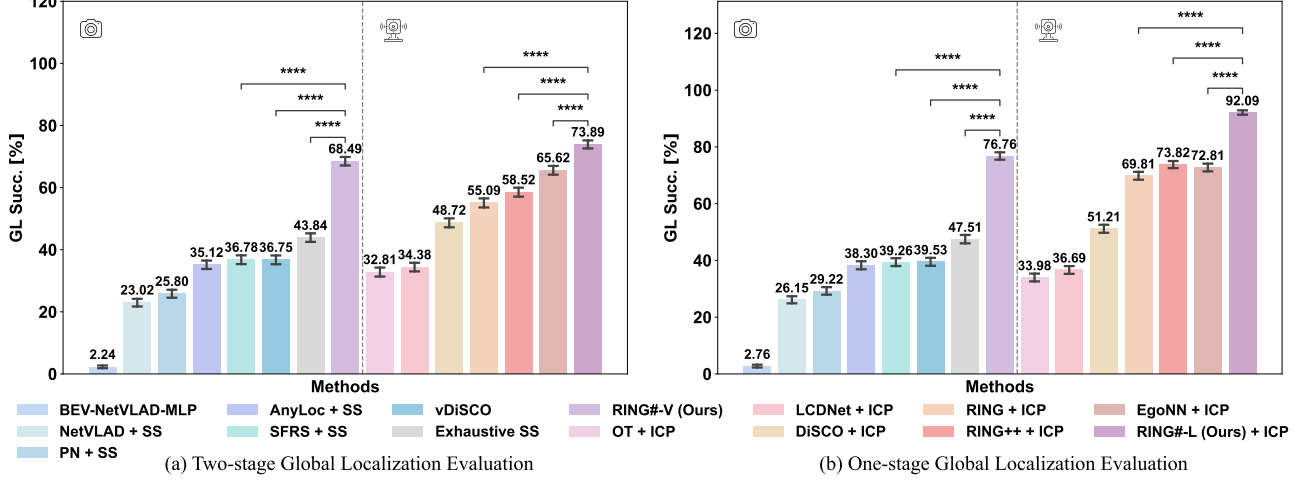


Fig. 11. **Two-stage and one-stage global localization success rate on the NCLT and Oxford datasets.** SS: SuperPoint + SuperGlue, PN: Patch-NetVLAD, OT: OverlapTransformer. The two-tailed Mann-Whitney U test shows statistical significance for a pair of methods comparison: \*  $P < 0.05$ ; \*\*  $P < 0.01$ ; \*\*\*  $P < 0.001$ ; \*\*\*\*  $P < 0.0001$ .

effective for RING#-V. Building on  $\mathcal{M}_7$ ,  $\mathcal{M}_8$  jointly trains both place recognition and pose estimation with specific losses, resulting in a 22% improvement in Recall@1 over  $\mathcal{M}_7$ . This demonstrates the benefits of integrating place recognition and pose estimation into a single network for *PR-then-PE localization*. However,  $\mathcal{M}_8$  still lags behind  $\mathcal{M}_6$  in both Recall@1 and PE Succ., which verifies the effectiveness of the proposed *PR-by-PE localization* paradigm.

**Map Interval.** To further investigate the influence of map intervals, we evaluate some representative methods using Protocol 3 on the NCLT dataset across varying map intervals. In addition to the 20m map interval used in the previous experiments, we evaluate the one-stage global localization performance of RING, RING++, EgoNN, RING#-V, and RING#-L at 30m, 40m, 50m, 60m, 70m, and 80m map intervals, as illustrated in Fig. 12. As expected, increasing the map interval reduces the overlap between the query and map keyframes and introduces greater viewpoint variation, causing a general performance decline across all methods. However, RING#-V and RING#-L exhibit remarkable robustness, consistently surpassing other methods across all intervals. Notably, RING#-V tested at larger intervals even outperforms other methods tested at the 20m interval, which highlights the inherent strengths of the *PR-by-PE localization* paradigm.

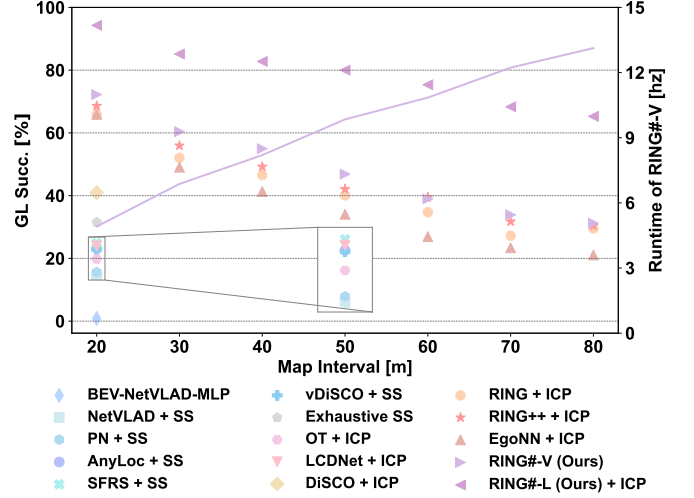


Fig. 12. **One-stage global localization success rate and runtime of RING#-V on the NCLT dataset at different map intervals.** SS: SuperPoint + SuperGlue, PN: Patch-NetVLAD, OT: OverlapTransformer. We display the GL Succ. of all methods at 20m map interval and the GL Succ. of RING, RING++, EgoNN, RING# at map intervals ranging from 30m to 80m.

### 1. Runtime Analysis

In this section, we evaluate the runtime of all approaches with an NVIDIA GeForce GTX 4090 GPU. We report the average runtime per query for all approaches on “2012-01-08”

TABLE VI  
ABLATION STUDY OF NETWORK ARCHITECTURE\*

Model	CNN in Branch I	CNN in Branch II	Depth Loss	PR Loss	PE Loss	Pose Refinement	Recall@1 ↑	RE [°] ↓	TE [m] ↓	PE Succ. ↑
$M_1$	<b>X</b>	<b>X</b>	<b>X</b>	<b>X</b>	<b>✓</b>	<b>X</b>	0.22	6.59 / 15.73	3.35 / 5.68	0.17
$M_2$	Before RT	Before RC	<b>X</b>	<b>X</b>	<b>✓</b>	<b>X</b>	0.56	2.40 / 5.70	1.76 / 3.78	0.51
$M_3$	After RT	Before RC	<b>X</b>	<b>X</b>	<b>✓</b>	<b>X</b>	0.59	2.10 / 3.81	1.19 / 2.70	0.65
$M_4$	After RT	After RC	<b>X</b>	<b>X</b>	<b>✓</b>	<b>X</b>	0.79	<u>2.07</u> / 4.24	1.04 / 2.07	0.69
$M_5$	After RT	After RC	<b>✓</b>	<b>X</b>	<b>✓</b>	<b>X</b>	<b>0.82</b>	2.27 / 4.10	<u>0.86</u> / 1.71	0.71
$M_6$ (Ours)	After RT	After RC	<b>✓</b>	<b>X</b>	<b>✓</b>	<b>✓</b>	<b>0.82</b>	<b>1.25</b> / <u>2.22</u>	<b>0.71</b> / <u>1.29</u>	<b>0.85</b>
$M_7$	After RT	After RC	<b>✓</b>	<b>✓</b>	<b>X</b>	<b>X</b>	0.32	-	-	-
$M_8$	After RT	After RC	<b>✓</b>	<b>✓</b>	<b>✓</b>	<b>✓</b>	0.54	<b>1.25</b> / <u>2.36</u>	0.98 / <u>1.56</u>	<u>0.83</u>

\* Branch I: Rotation Branch, Branch II: Translation Branch, PR Loss: Place Recognition Loss, PE Loss: Pose Estimation Loss, Pose Refinement: 3-DoF Exhaustive Matching upon Neural BEV, RT: Radon Transform, RC: Rotation Compensation. We report 50th and 75th percentile errors for RE and TE. The best result is highlighted in **bold** and the second best is underlined.

to “2012-08-20” of the NCLT dataset in Fig. 13. The vision baselines except for BEV-NetVLAD-MLP exhibit substantial runtime due to the extensive time required for detecting and matching local features across multi-view images using SuperPoint and SuperGlue for pose estimation. Among these, Exhaustive SS has the longest runtime due to its exhaustive matching process between the query and all map keyframes. Although BEV-NetVLAD-MLP demonstrates the shortest runtime, it is unable to estimate accurate poses. In contrast, RING#-V achieves a feasible runtime while maintaining superior performance, thanks to its end-to-end design, which leverages a fast correlation algorithm and batch processing on GPU. Among LiDAR-based approaches, although OverlapTransformer and DiSCO are faster than other approaches, they fail to provide accurate initial poses for ICP alignment. In contrast, RING#-L takes comparable runtime while has the best performance. Moreover, as shown in Table II, RING#-L achieves nearly identical performance with or without ICP, allowing for reduced iterations to save time when necessary.

Table VII details the runtime of each module within RING#. The feature extraction time represents the generation time of two equivariant representations in the rotation and translation branches. The exhaustive search time, which is the most time-consuming part of RING#, reports the time needed to calculate similarities between the query and all map keyframes in the database and identify the most similar one. The pose refinement time of RING#-V is the time of pose refinement via 3-DoF exhaustive matching. Due to the larger grid size of the LiDAR BEV representation, RING#-L requires more time than RING#-V. Additionally, we investigate how the runtime of RING#-V changes with different map intervals in Fig. 12. As the map size increases (*i.e.* the map interval decreases), both runtime and performance increase empirically. To achieve a balance between performance and runtime, the map interval can be adjusted based on the specific application requirements.

## VII. CONCLUSION AND FUTURE WORK

In this paper, we propose RING#, an end-to-end *PR-by-PE localization* framework in the BEV space. By correlation-based exhaustive search on equivariant BEV representations, RING# effectively captures the spatial structure of the environment, enabling globally convergent localization for both

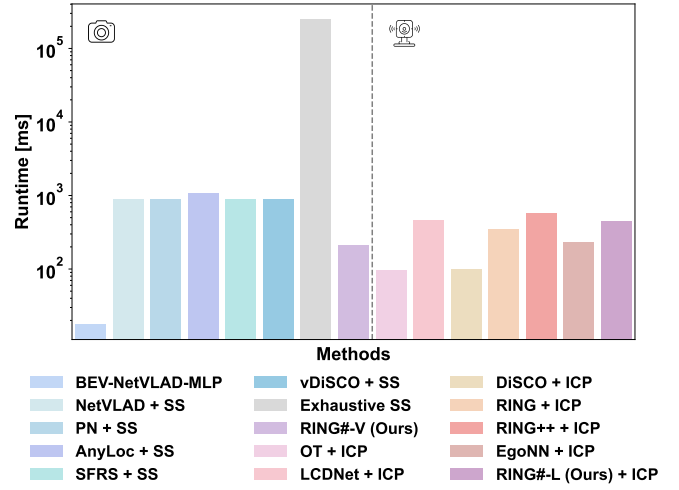


Fig. 13. Average runtime per query of all methods on the NCLT dataset. SS: SuperPoint + SuperGlue, PN: Patch-NetVLAD, OT: OverlapTransformer.

TABLE VII  
RUNTIME OF EACH RING# MODULE

Approach	Feature Extraction [ms]	Exhaustive Search [ms]	Pose Refinement [ms]
RING#-V	12.64	152.92	44.22
RING#-L	16.31	330.01	-

vision and LiDAR modalities. Extensive experiments on the NCLT and Oxford datasets demonstrate its superior localization performance, especially under challenging environmental variations. The success of RING# not only confirms the viability of the *PR-by-PE localization* paradigm but also sets a new standard for localization performance, emphasizing the potential of our method in the realm of autonomous navigation and robotic systems.

**Limitations and Future Work.** While RING# excels in 3-DoF localization, this may be insufficient for some applications. We expect to extend RING# to 6-DoF localization in the future. Additionally, the framework’s adaptability to various sensor setups remains an area for further research. Exploring the integration of foundation models into our approach, while preserving the critical equivariant properties, presents a promising direction to enhance generalization and further advance the state-of-the-art of global localization.

## REFERENCES

[1] M. Cummins and P. Newman, “Fab-map: Probabilistic localization and mapping in the space of appearance,” *Intl. Journal of Robotics Research (IJRR)*, vol. 27, no. 6, pp. 647–665, 2008.

[2] ——, “Appearance-only slam at large scale with fab-map 2.0,” *Intl. Journal of Robotics Research (IJRR)*, vol. 30, no. 9, pp. 1100–1123, 2011.

[3] M. J. Milford and G. F. Wyeth, “Seqslam: Visual route-based navigation for sunny summer days and stormy winter nights,” in *Proc. of the IEEE Intl. Conf. on Robotics & Automation (ICRA)*, 2012, pp. 1643–1649.

[4] R. Mur-Artal, J. M. M. Montiel, and J. D. Tardos, “Orb-slam: a versatile and accurate monocular slam system,” *IEEE Trans. on Robotics (TRO)*, vol. 31, no. 5, pp. 1147–1163, 2015.

[5] S. Lowry, N. Sünderauf, P. Newman, J. J. Leonard, D. Cox, P. Corke, and M. J. Milford, “Visual place recognition: A survey,” *IEEE Trans. on Robotics (TRO)*, vol. 32, no. 1, pp. 1–19, 2015.

[6] A. Angeli, D. Filliat, S. Doncieux, and J.-A. Meyer, “Fast and incremental method for loop-closure detection using bags of visual words,” *IEEE Trans. on Robotics (TRO)*, vol. 24, no. 5, pp. 1027–1037, 2008.

[7] R. Arandjelovic and A. Zisserman, “All about vlad,” in *Proc. of the IEEE Conf. on Computer Vision and Pattern Recognition (CVPR)*, 2013, pp. 1578–1585.

[8] D. Gálvez-López and J. D. Tardos, “Bags of binary words for fast place recognition in image sequences,” *IEEE Trans. on Robotics (TRO)*, vol. 28, no. 5, pp. 1188–1197, 2012.

[9] R. Arandjelovic, P. Gronat, A. Torii, T. Pajdla, and J. Sivic, “Netvlad: Cnn architecture for weakly supervised place recognition,” in *Proc. of the IEEE Conf. on Computer Vision and Pattern Recognition (CVPR)*, 2016, pp. 5297–5307.

[10] Y. Ge, H. Wang, F. Zhu, R. Zhao, and H. Li, “Self-supervising fine-grained region similarities for large-scale image localization,” in *Proc. of the Europ. Conf. on Computer Vision (ECCV)*, 2020, pp. 369–386.

[11] S. Hausler, S. Garg, M. Xu, M. Milford, and T. Fischer, “Patch-netvlad: Multi-scale fusion of locally-global descriptors for place recognition,” in *Proc. of the IEEE/CVF Conf. on Computer Vision and Pattern Recognition (CVPR)*, 2021, pp. 14 141–14 152.

[12] N. Keetha, A. Mishra, J. Karhade, K. M. Jatavallabhula, S. Scherer, M. Krishna, and S. Garg, “Anyloc: Towards universal visual place recognition,” *IEEE Robotics and Automation Letters (RA-L)*, 2023.

[13] A. Ali-Bey, B. Chaib-Draa, and P. Giguere, “Mixvpr: Feature mixing for visual place recognition,” in *Proc. of the IEEE Winter Conf. on Applications of Computer Vision (WACV)*, 2023, pp. 2998–3007.

[14] L. He, X. Wang, and H. Zhang, “M2dp: A novel 3d point cloud descriptor and its application in loop closure detection,” in *Proc. of the IEEE/RSJ Intl. Conf. on Intelligent Robots and Systems (IROS)*, 2016, pp. 231–237.

[15] M. A. Uy and G. H. Lee, “Pointnetvlad: Deep point cloud based retrieval for large-scale place recognition,” in *Proc. of the IEEE Conf. on Computer Vision and Pattern Recognition (CVPR)*, 2018, pp. 4470–4479.

[16] J. Ma, J. Zhang, J. Xu, R. Ai, W. Gu, and X. Chen, “Overlaptransformer: An efficient and yaw-angle-invariant transformer network for lidar-based place recognition,” *IEEE Robotics and Automation Letters (RA-L)*, vol. 7, no. 3, pp. 6958–6965, 2022.

[17] S. Lu, X. Xu, L. Tang, R. Xiong, and Y. Wang, “Deepring: Learning roto-translation invariant representation for lidar based place recognition,” in *Proc. of the IEEE Intl. Conf. on Robotics & Automation (ICRA)*, 2023, pp. 1904–1911.

[18] M. A. Fischler and R. C. Bolles, “Random sample consensus: a paradigm for model fitting with applications to image analysis and automated cartography,” *Communications of the ACM*, vol. 24, no. 6, pp. 381–395, 1981.

[19] O. Chum, J. Matas, and J. Kittler, “Locally optimized ransac,” in *Pattern Recognition*, 2003, pp. 236–243.

[20] O. Chum and J. Matas, “Matching with prosac-progressive sample consensus,” in *Proc. of the IEEE Conf. on Computer Vision and Pattern Recognition (CVPR)*, vol. 1, 2005, pp. 220–226.

[21] L. Cavalli, V. Larsson, M. R. Oswald, T. Sattler, and M. Pollefeys, “Adalam: Revisiting handcrafted outlier detection,” *arXiv preprint arXiv:2006.04250*, 2020.

[22] P. J. Besl and N. D. McKay, “Method for registration of 3-d shapes,” in *Sensor fusion IV: control paradigms and data structures*, vol. 1611, 1992, pp. 586–606.

[23] C. Shi, X. Chen, H. Lu, W. Deng, J. Xiao, and B. Dai, “Rdmnet: Reliable dense matching based point cloud registration for autonomous driving,” *IEEE Trans. on Intelligent Transportation Systems (T-ITS)*, 2023.

[24] C. Shi, X. Chen, J. Xiao, B. Dai, and H. Lu, “Fast and accurate deep loop closing and relocalization for reliable lidar slam,” *IEEE Trans. on Robotics (TRO)*, 2024.

[25] P.-E. Sarlin, F. Debraine, M. Dymczyk, R. Siegwart, and C. Cadena, “Leveraging deep visual descriptors for hierarchical efficient localization,” in *Proc. of the Conf. on Robot Learning (CoRL)*, 2018, pp. 456–465.

[26] P.-E. Sarlin, C. Cadena, R. Siegwart, and M. Dymczyk, “From coarse to fine: Robust hierarchical localization at large scale,” in *Proc. of the IEEE/CVF Conf. on Computer Vision and Pattern Recognition (CVPR)*, 2019, pp. 12 716–12 725.

[27] J. Du, R. Wang, and D. Cremers, “Dh3d: Deep hierarchical 3d descriptors for robust large-scale 6dof relocalization,” in *Proc. of the Europ. Conf. on Computer Vision (ECCV)*, 2020, pp. 744–762.

[28] X. Chen, T. Läbe, A. Milioto, T. Röhling, J. Behley, and C. Stachniss, “Overlapnet: A siamese network for computing lidar scan similarity with applications to loop closing and localization,” *Autonomous Robots*, vol. 46, pp. 61–81, 2021.

[29] X. Xu, H. Yin, Z. Chen, Y. Li, Y. Wang, and R. Xiong, “Disco: Differentiable scan context with orientation,” *IEEE Robotics and Automation Letters (RA-L)*, vol. 6, no. 2, pp. 2791–2798, 2021.

[30] J. Komorowski, M. Wysoczanska, and T. Trzcinski, “Egonn: Egocentric neural network for point cloud based 6dof relocalization at the city scale,” *IEEE Robotics and Automation Letters (RA-L)*, vol. 7, no. 2, pp. 722–729, 2021.

[31] D. Cattaneo, M. Vaghi, and A. Valada, “Lcdnet: Deep loop closure detection and point cloud registration for lidar slam,” *IEEE Trans. on Robotics (TRO)*, vol. 38, no. 4, pp. 2074–2093, 2022.

[32] T. Sattler, B. Leibe, and L. Kobbelt, “Improving image-based localization by active correspondence search,” in *Proc. of the Europ. Conf. on Computer Vision (ECCV)*, 2012, pp. 752–765.

[33] P.-E. Sarlin, D. DeTone, T. Malisiewicz, and A. Rabinovich, “Superglue: Learning feature matching with graph neural networks,” in *Proc. of the IEEE/CVF Conf. on Computer Vision and Pattern Recognition (CVPR)*, 2020, pp. 4938–4947.

[34] W. Jiang, E. Trulls, J. Hosang, A. Tagliasacchi, and K. M. Yi, “Cotr: Correspondence transformer for matching across images,” in *Proc. of the IEEE/CVF Intl. Conf. on Computer Vision (ICCV)*, 2021, pp. 6207–6217.

[35] J. Sun, Z. Shen, Y. Wang, H. Bao, and X. Zhou, “Loft: Detector-free local feature matching with transformers,” in *Proc. of the IEEE/CVF Conf. on Computer Vision and Pattern Recognition (CVPR)*, 2021, pp. 8922–8931.

[36] Q. Wang, J. Zhang, K. Yang, K. Peng, and R. Stiefelhagen, “Matchformer: Interleaving attention in transformers for feature matching,” in *Proc. of the Asian Conf. on Computer Vision (ACCV)*, 2022, pp. 2746–2762.

[37] X. Xu, S. Lu, J. Wu, H. Lu, Q. Zhu, Y. Liao, R. Xiong, and Y. Wang, “Ring++: Roto-translation-invariant gram for global localization on a sparse scan map,” *IEEE Trans. on Robotics (TRO)*, 2023.

[38] D. G. Lowe, “Distinctive image features from scale-invariant keypoints,” *Proc. of the IEEE Intl. Conf. on Computer Vision (ICCV)*, vol. 60, pp. 91–110, 2004.

[39] H. Bay, T. Tuytelaars, and L. V. Gool, “Surf: Speeded up robust features,” in *Proc. of the Europ. Conf. on Computer Vision (ECCV)*, 2006, pp. 404–417.

[40] E. Rublee, V. Rabaud, K. Konolige, and G. Bradski, “Orb: An efficient alternative to sift or surf,” in *Proc. of the IEEE Intl. Conf. on Computer Vision (ICCV)*, 2011, pp. 2564–2571.

[41] F. Perronnin and C. Dance, “Fisher kernels on visual vocabularies for image categorization,” in *Proc. of the IEEE Conf. on Computer Vision and Pattern Recognition (CVPR)*, 2007, pp. 1–8.

[42] F. Perronnin, Y. Liu, J. Sánchez, and H. Poirier, “Large-scale image retrieval with compressed fisher vectors,” in *Proc. of the IEEE Conf. on Computer Vision and Pattern Recognition (CVPR)*, 2010, pp. 3384–3391.

[43] D. DeTone, T. Malisiewicz, and A. Rabinovich, “Superpoint: Self-supervised interest point detection and description,” in *Proc. of the IEEE/CVF Conf. on Computer Vision and Pattern Recognition Workshops*, 2018, pp. 224–236.

[44] J. Revaud, C. De Souza, M. Humenberger, and P. Weinzaepfel, “R2d2: Reliable and repeatable detector and descriptor,” *Proc. of the Advances in Neural Information Processing Systems (NIPS)*, vol. 32, 2019.

[45] Y.-Y. Jau, R. Zhu, H. Su, and M. Chandraker, “Deep keypoint-based camera pose estimation with geometric constraints,” in *Proc. of the IEEE/RSJ Intl. Conf. on Intelligent Robots and Systems (IROS)*, 2020, pp. 4950–4957.

[46] F. Radenović, G. Tolias, and O. Chum, “Fine-tuning cnn image retrieval with no human annotation,” *IEEE Trans. on Pattern Analysis and Machine Intelligence (TPAMI)*, vol. 41, no. 7, pp. 1655–1668, 2018.

[47] G. Peng, J. Zhang, H. Li, and D. Wang, “Attentional pyramid pooling of salient visual residuals for place recognition,” in *Proc. of the IEEE/CVF Intl. Conf. on Computer Vision (ICCV)*, 2021, pp. 885–894.

[48] R. Wang, Y. Shen, W. Zuo, S. Zhou, and N. Zheng, “Transvr: Transformer-based place recognition with multi-level attention aggregation,” in *Proc. of the IEEE/CVF Conf. on Computer Vision and Pattern Recognition (CVPR)*, 2022, pp. 13 648–13 657.

[49] S. S. Kannan and B.-C. Min, “Placeformer: Transformer-based visual place recognition using multi-scale patch selection and fusion,” *arXiv preprint arXiv:2401.13082*, 2024.

[50] G. Barbarani, M. Mostafa, H. Bayramov, G. Trivigno, G. Berton, C. Masone, and B. Caputo, “Are local features all you need for cross-domain visual place recognition?” in *Proc. of the IEEE/CVF Conf. on Computer Vision and Pattern Recognition (CVPR)*, 2023, pp. 6154–6164.

[51] S. Zhu, L. Yang, C. Chen, M. Shah, X. Shen, and H. Wang, “R2former: Unified retrieval and reranking transformer for place recognition,” in *Proc. of the IEEE/CVF Conf. on Computer Vision and Pattern Recognition (CVPR)*, 2023, pp. 19 370–19 380.

[52] G. Kim and A. Kim, “Scan context: Egocentric spatial descriptor for place recognition within 3d point cloud map,” in *Proc. of the IEEE/RSJ Intl. Conf. on Intelligent Robots and Systems (IROS)*, 2018, pp. 4802–4809.

[53] H. Wang, C. Wang, and L. Xie, “Intensity scan context: Coding intensity and geometry relations for loop closure detection,” in *Proc. of the IEEE Intl. Conf. on Robotics & Automation (ICRA)*, 2020, pp. 2095–2101.

[54] Y. Wang, Z. Sun, C.-Z. Xu, S. E. Sarma, J. Yang, and H. Kong, “Lidar iris for loop-closure detection,” in *Proc. of the IEEE/RSJ Intl. Conf. on Intelligent Robots and Systems (IROS)*, 2020, pp. 5769–5775.

[55] G. Kim, S. Choi, and A. Kim, “Scan context++: Structural place recognition robust to rotation and lateral variations in urban environments,” *IEEE Trans. on Robotics (TRO)*, 2021.

[56] L. Li, X. Kong, X. Zhao, T. Huang, W. Li, F. Wen, H. Zhang, and Y. Liu, “Ssc: Semantic scan context for large-scale place recognition,” in *Proc. of the IEEE/RSJ Intl. Conf. on Intelligent Robots and Systems (IROS)*, 2021, pp. 2092–2099.

[57] S. Lu, X. Xu, H. Yin, Z. Chen, R. Xiong, and Y. Wang, “One ring to rule them all: Radon sinogram for place recognition, orientation and translation estimation,” in *Proc. of the IEEE/RSJ Intl. Conf. on Intelligent Robots and Systems (IROS)*, 2022, pp. 2778–2785.

[58] Y. Cui, X. Chen, Y. Zhang, J. Dong, Q. Wu, and F. Zhu, “Bow3d: Bag of words for real-time loop closing in 3d lidar slam,” *IEEE Robotics and Automation Letters (RA-L)*, vol. 8, no. 5, pp. 2828–2835, 2022.

[59] Y. Cui, Y. Zhang, J. Dong, H. Sun, X. Chen, and F. Zhu, “Link3d: Linear keypoints representation for 3d lidar point cloud,” *IEEE Robotics and Automation Letters (RA-L)*, 2024.

[60] C. R. Qi, H. Su, K. Mo, and L. J. Guibas, “Pointnet: Deep learning on point sets for 3d classification and segmentation,” in *Proc. of the IEEE Conf. on Computer Vision and Pattern Recognition (CVPR)*, 2017, pp. 652–660.

[61] K. Vidanapathirana, P. Moghadam, S. Sridharan, and C. Fookes, “Spectral geometric verification: Re-ranking point cloud retrieval for metric localization,” *IEEE Robotics and Automation Letters (RA-L)*, vol. 8, no. 5, pp. 2494–2501, 2023.

[62] J. Philion and S. Fidler, “Lift, splat, shoot: Encoding images from arbitrary camera rigs by implicitly unprojecting to 3d,” in *Proc. of the Europ. Conf. on Computer Vision (ECCV)*, 2020, pp. 194–210.

[63] J. Huang, G. Huang, Z. Zhu, Y. Ye, and D. Du, “Bevdet: High-performance multi-camera 3d object detection in bird-eye-view,” *arXiv preprint arXiv:2112.11790*, 2021.

[64] Y. Li, Z. Ge, G. Yu, J. Yang, Z. Wang, Y. Shi, J. Sun, and Z. Li, “Bevdepth: Acquisition of reliable depth for multi-view 3d object detection,” in *Proceedings of the AAAI Conference on Artificial Intelligence*, vol. 37, no. 2, 2023, pp. 1477–1485.

[65] Y. Wang, V. C. Guizilini, T. Zhang, Y. Wang, H. Zhao, and J. Solomon, “Detr3d: 3d object detection from multi-view images via 3d-to-2d queries,” in *Proc. of the Conf. on Robot Learning (CoRL)*, 2022, pp. 180–191.

[66] Y. Liu, T. Wang, X. Zhang, and J. Sun, “Petr: Position embedding transformation for multi-view 3d object detection,” in *Proc. of the Europ. Conf. on Computer Vision (ECCV)*, 2022, pp. 531–548.

[67] Z. Li, W. Wang, H. Li, E. Xie, C. Sima, T. Lu, Y. Qiao, and J. Dai, “Bevformer: Learning bird’s-eye-view representation from multi-camera images via spatiotemporal transformers,” in *Proc. of the Europ. Conf. on Computer Vision (ECCV)*, 2022, pp. 1–18.

[68] C. Yang, Y. Chen, H. Tian, C. Tao, X. Zhu, Z. Zhang, G. Huang, H. Li, Y. Qiao, L. Lu *et al.*, “Bevformer v2: Adapting modern image backbones to bird’s-eye-view recognition via perspective supervision,” in *Proc. of the IEEE/CVF Conf. on Computer Vision and Pattern Recognition (CVPR)*, 2023, pp. 17 830–17 839.

[69] W. Lu, Y. Zhou, G. Wan, S. Hou, and S. Song, “L3-net: Towards learning based lidar localization for autonomous driving,” in *Proc. of the IEEE/CVF Conf. on Computer Vision and Pattern Recognition (CVPR)*, June 2019.

[70] P.-E. Sarlin, E. Trulls, M. Pollefeys, J. Hosang, and S. Lynen, “Snap: Self-supervised neural maps for visual positioning and semantic understanding,” *Proc. of the Advances in Neural Information Processing Systems (NIPS)*, vol. 36, 2024.

[71] S. R. Deans, *The Radon transform and some of its applications*. Courier Corporation, 2007.

[72] R. Matungka, Y. F. Zheng, and R. L. Ewing, “Image registration using adaptive polar transform,” *IEEE Trans. on Image Processing*, vol. 18, no. 10, pp. 2340–2354, 2009.

[73] E. O. Brigham, *The fast Fourier transform and its applications*. Prentice-Hall, Inc., 1988.

[74] K. He, X. Zhang, S. Ren, and J. Sun, “Deep residual learning for image recognition,” in *Proc. of the IEEE Conf. on Computer Vision and Pattern Recognition (CVPR)*, 2016, pp. 770–778.

[75] M. Weiler and G. Cesa, “General E(2)-Equivariant Steerable CNNs,” in *Proc. of the Conf. on Neural Information Processing Systems (NeurIPS)*, 2019.

[76] K. Koide, M. Yokozuka, S. Oishi, and A. Banno, “Voxelized gicp for fast and accurate 3d point cloud registration,” in *Proc. of the IEEE Intl. Conf. on Robotics & Automation (ICRA)*, 2021, pp. 11 054–11 059.

[77] N. Carlevaris-Bianco, A. K. Ushani, and R. M. Eustice, “University of michigan north campus long-term vision and lidar dataset,” *Intl. Journal of Robotics Research (IJRR)*, vol. 35, no. 9, pp. 1023–1035, 2016.

[78] D. Barnes, M. Gadd, P. Murcatt, P. Newman, and I. Posner, “The oxford radar robotcar dataset: A radar extension to the oxford robotcar dataset,” in *Proc. of the IEEE Intl. Conf. on Robotics & Automation (ICRA)*, 2020, pp. 6433–6438.

[79] W. Maddern, G. Pascoe, C. Linegar, and P. Newman, “1 year, 1000 km: The oxford robotcar dataset,” *Intl. Journal of Robotics Research (IJRR)*, vol. 36, no. 1, pp. 3–15, 2017.

[80] A. Paszke, S. Gross, F. Massa, A. Lerer, J. Bradbury, G. Chanan, T. Killeen, Z. Lin, N. Gimelshein, L. Antiga *et al.*, “Pytorch: An imperative style, high-performance deep learning library,” *Proc. of the Advances in Neural Information Processing Systems (NIPS)*, vol. 32, 2019.

[81] D. P. Kingma and J. Ba, “Adam: A method for stochastic optimization,” *arXiv preprint arXiv:1412.6980*, 2014.

[82] J. Komorowski, “Minkloc3d: Point cloud based large-scale place recognition,” in *Proceedings of the IEEE/CVF Winter Conference on Applications of Computer Vision*, 2021, pp. 1790–1799.

[83] X. Xu, Y. Jiao, S. Lu, X. Ding, R. Xiong, and Y. Wang, “Leveraging bev representation for 360-degree visual place recognition,” *arXiv preprint arXiv:2305.13814*, 2023.

[84] M. Oquab, T. Darret, T. Moutakanni, H. Vo, M. Szafraniec, V. Khalidov, P. Fernandez, D. Haziza, F. Massa, A. El-Nouby *et al.*, “Dinov2: Learning robust visual features without supervision,” *arXiv preprint arXiv:2304.07193*, 2023.

[85] L. Kneip, D. Scaramuzza, and R. Siegwart, “A novel parametrization of the perspective-three-point problem for a direct computation of absolute camera position and orientation,” in *Proc. of the IEEE Conf. on Computer Vision and Pattern Recognition (CVPR)*, 2011, pp. 2969–2976.

[86] P. E. McKnight and J. Najab, “Mann-whitney u test,” *The Corsini encyclopedia of psychology*, pp. 1–1, 2010.

### VIII. APPENDIX

This appendix presents additional details and visualizations that supplement the main text, providing further qualitative results, performance insights, and failure cases analysis.

#### A. Additional Results of Place Recognition

In addition to the visualization of top 1 retrieved matches for the NCLT dataset shown in Fig. 4, we provide additional qualitative results for the Oxford dataset in Fig. 14. The overall performance on the Oxford dataset surpasses that on the NCLT dataset, primarily due to fewer environmental changes in the Oxford dataset. Compared to state-of-the-art methods, RING#-V and RING#-L achieve a higher number of correct matches and fewer incorrect matches, demonstrating the superior performance of our method. This is consistent with the quantitative findings discussed in Sec. VI-D.

#### B. Additional Results of Global Localization

While Sec. VI-G focuses on the quantitative evaluation of global localization performance, we provide additional qualitative results on both the NCLT and Oxford datasets. For the NCLT dataset, Fig. 15 and Fig. 16 illustrate the global localization results for RING#-V compared with Exhaustive SS and RING#-L compared with EgoNN. Similarly, for the Oxford dataset, Fig. 17 and Fig. 18 depict the global localization results for RING#-V versus Exhaustive SS and RING#-L versus EgoNN. In these figures, topological nodes are represented in gray, with the ground truth indicated in green.

As depicted in Fig. 15 and Fig. 16, it is evident that these methods struggle in accurately localizing the robot in scenarios with significant viewpoint changes (*e.g.* large turns or backward movements in the trajectory). In contrast, Fig. 17 and Fig. 18 demonstrate that the global localization results on the Oxford dataset are more accurate due to less significant variations in viewpoint and environment. Despite the challenging scenarios and sparse topological nodes, RING#-V and RING#-L outperform other methods on both datasets, showcasing the

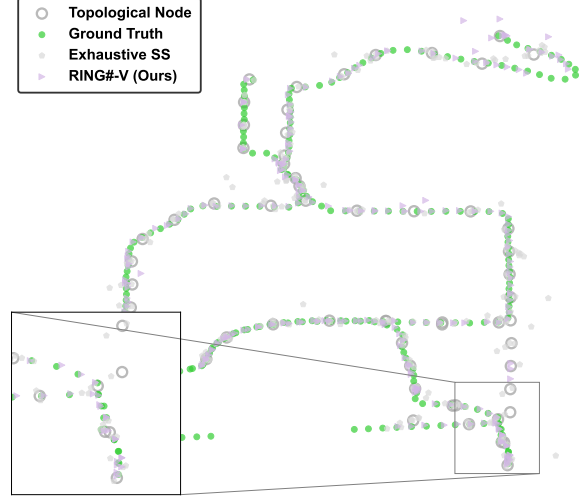


Fig. 15. **Global localization result of RING#-V on the NCLT dataset.** The topological nodes are sparse and shown as gray, the ground truth is shown in green, and the prediction is shown in blue.

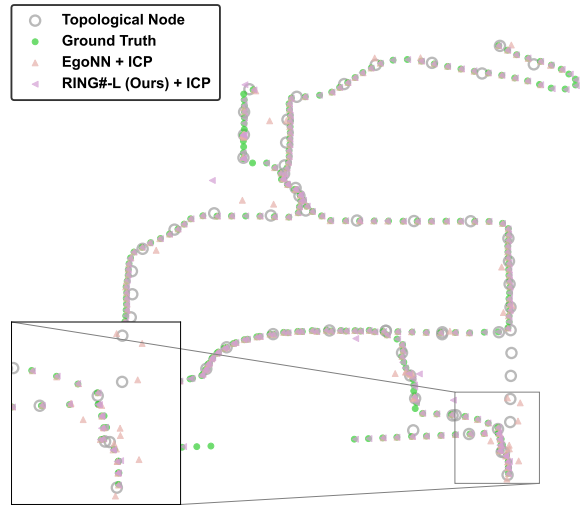


Fig. 16. **Global localization result of RING#-L on the NCLT dataset.** The topological nodes are sparse and shown as gray, the ground truth is shown in green, and the prediction is shown in blue.

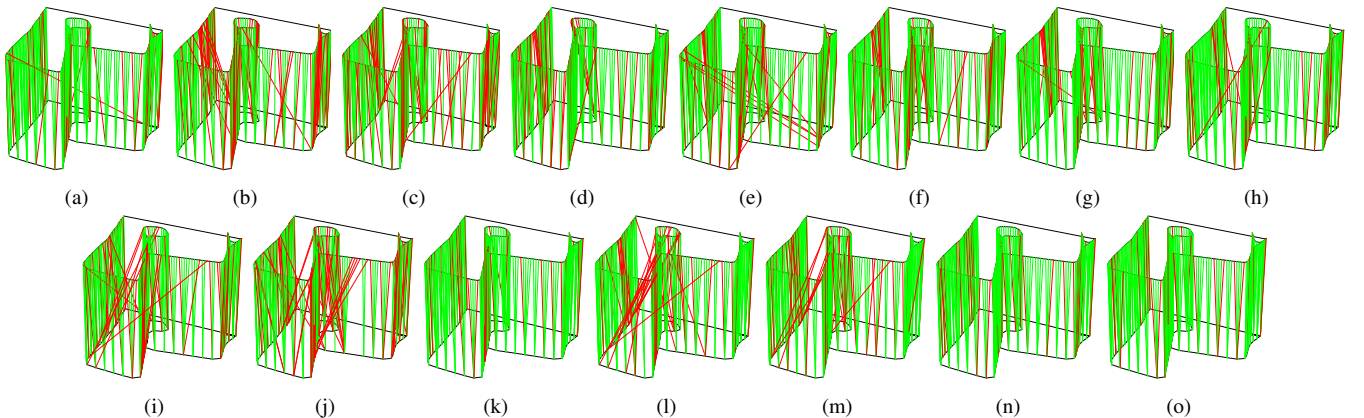


Fig. 14. **Top 1 retrieved matches for protocol 1 on the Oxford dataset.** (a) Exhaustive SS [33], [43]. (b) NetVLAD [9]. (c) Patch-NetVLAD [11]. (d) AnyLoc [12]. (e) SFRS [10]. (f) BEV-NetVLAD-MLP. (g) vDiSCO [83]. (h) RING#-V (Ours). (i) OverlapTransformer [16]. (j) LCDNet [31]. (k) DiSCO [29]. (l) RING [57]. (m) RING++ [37]. (n) EgoNN [30]. (o) RING#-L (Ours). The black line — represents the trajectory, the green line — represents the correct retrieval match, and the red line — represents the wrong retrieval match.

effectiveness of our approach. Specifically, RING#-L benefits from explicit geometric constraints, allowing it to outperform RING#-V, particularly on the NCLT dataset.

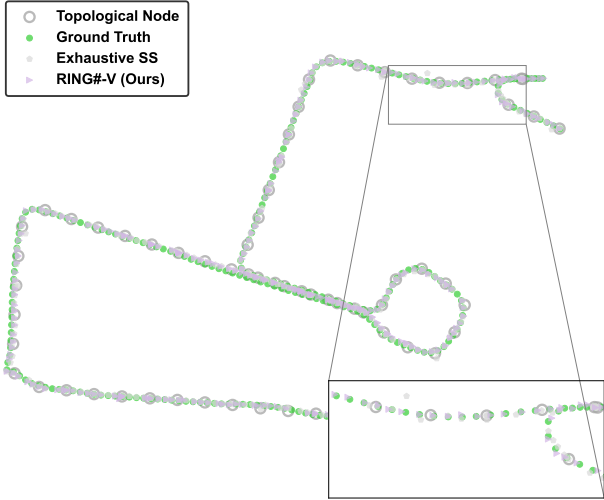


Fig. 17. **Global localization result of RING#-V on the Oxford dataset.** The topological nodes are sparse and shown as gray, the ground truth is shown in green, and the prediction is shown in blue.

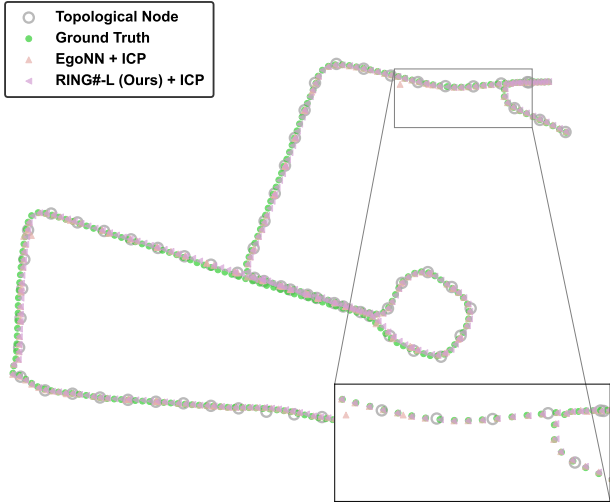


Fig. 18. **Global localization result of RING#-L on the Oxford dataset.** The topological nodes are sparse and shown as gray, the ground truth is shown in green, and the prediction is shown in blue.

### C. Failure Cases Analysis

We conduct a detailed analysis of failure cases for RING# where  $RE \geq 5^\circ$  and  $TE \geq 2m$  on the NCLT and Oxford datasets. Fig. 19 illustrates representative examples of failure cases for both RING#-V and RING#-L, with successful cases marked by right symbols and failed cases indicated by wrong symbols.

Failure cases primarily stem from the incorrect estimation of the rotation angle  $\hat{\theta}$  or the translation vector  $(\hat{x}, \hat{y})$ . Specifically, RING#-V has shown vulnerabilities in environments with significant lighting variations, which affect feature extraction. On the other hand, RING#-L struggles in environments characterized by repetitive structures, such as long, uniform

corridors. In such scenarios, LiDAR scans may appear similar across different sections, leading to localization ambiguities.

To address these limitations, future work could explore incorporating additional contextual information or employing multi-modal data fusion techniques. Combining vision and LiDAR data could enhance the ability of our approach to disambiguate challenging environments and improve overall robustness. By addressing these issues, the accuracy and reliability of RING# can be further improved, making it more effective across a broader range of scenarios.

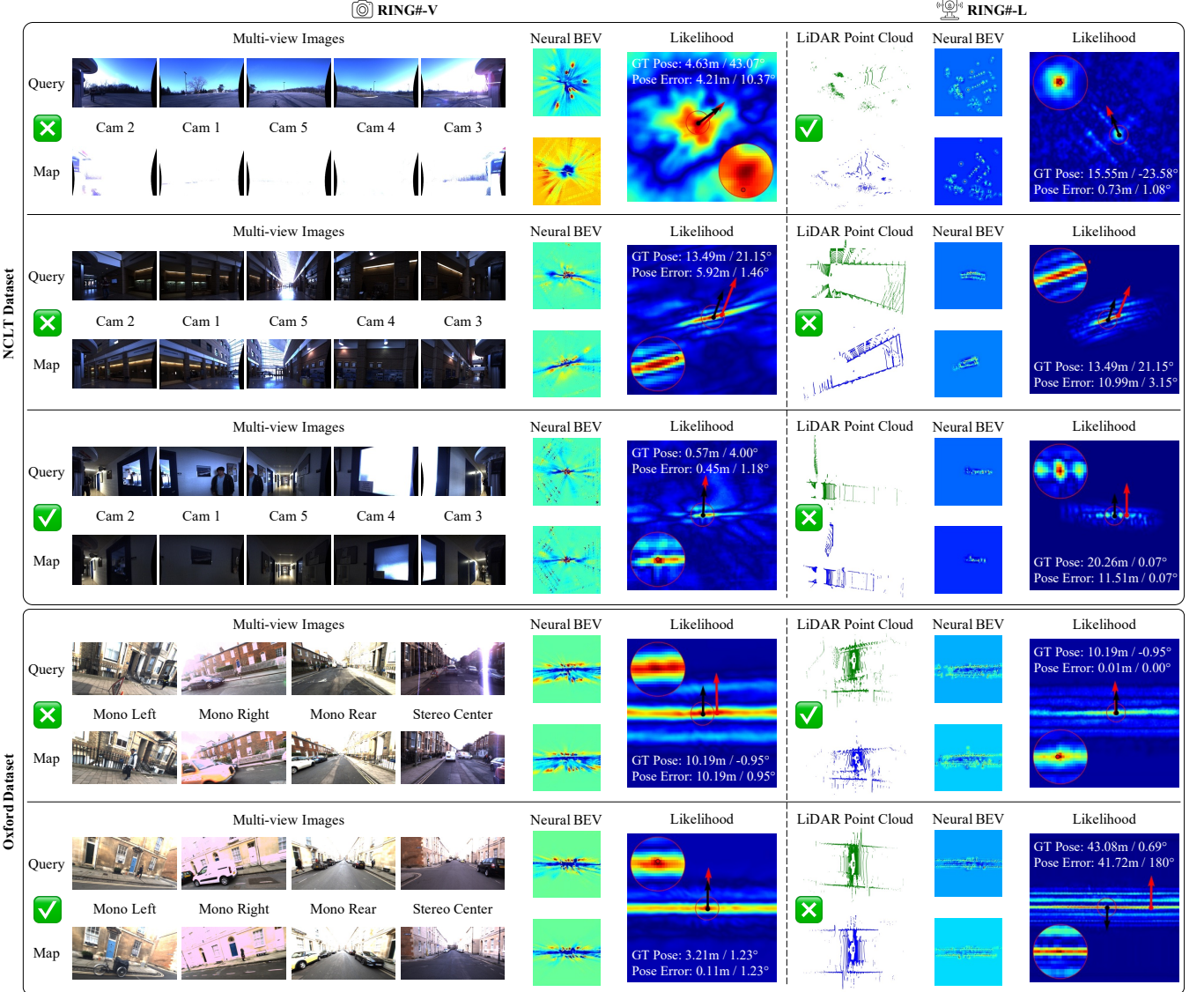


Fig. 19. **Failure localization cases of RING#-V and RING#-L.** We display several failure cases of RING#. On the likelihood plot, the black arrow  $\rightarrow$  shows the pose estimated by RING#, the red arrow  $\rightarrow$  shows the ground truth pose and the red dot  $\bullet$  shows the ground truth position. Here we rotate the query neural BEV by  $\hat{\theta}$  estimated using RING# to visualize the neural BEV under a 3-DoF pose transformation.